

Statistical properties of ^{233}U

*Investigating the Scissor Resonance of
 ^{233}U , using γSF and NLD from the Oslo
Method analysis with the new OMpy
software*

Tellef Storebakken



Thesis submitted for the degree of
Master in Nuclear and Energy Physics
60 credits

Department of Physics
The Faculty of Mathematics and Natural Sciences

UNIVERSITY OF OSLO

Spring 2021

© 2021 Tellef Storebakken

Statistical properties of ^{233}U

<http://www.duo.uio.no/>

Printed: Reprocentralen, University of Oslo

Statistical properties of ^{233}U

*Investigating the Scissor Resonance of ^{233}U ,
using γSF and NLD from the Oslo Method
analysis with the new OMpy software*

Tellef Storebakken

Abstract

In the presented work the Oslo method analysis is utilized to find the nuclear level density (NLD) and γ -ray strength (γ SF) function of ^{233}U from the $^{233}\text{U}(\alpha, \alpha')$ reaction. The γ SF is compared to previous data and in turn, used to extract the scissors resonance (SR) of ^{233}U .

The Oslo method analysis is conducted with the new Oslo method Python implementation (OMpy) together with the standard Oslo method software (OMS). This work is the first Oslo method analysis with the new OMpy software, independent from its creators. Bins with zero counts in the raw (E_γ, E_x) coincidence matrix are treated differently with the two software implementations. In OMpy, these bins end up being the most certain experimental data, creating difficulties in further statistical analysis of the SR mode. Two different methods of working around this problem have been investigated. One method was to create a larger dispersion in the first-generation matrix to level out these bins. With this method, the two implementations were on good agreement in regions with > 10 counts per energy bin in the (E_γ, E_x) coincidence matrix. Another method was to remove the γ SF points which emerged from the zero-count bins in further analysis of the SR mode.

Because of uncertain, and lack of, data in the E_γ energy region between 4-10 MeV for the γ SF and hence the difficulty of fitting higher-lying resonances, several methods of extracting the SR mode are presented. The resulting $B_{SR}(\text{M1})$ strengths deviate between $7.2\text{-}12.6 \mu_N^2$, but agree within their errorbars. Additionally, the ω_{SR} peak centroids are in good agreement at approximately 2.1 MeV, indicating the presence of a scissors resonance in the deformed ^{233}U nucleus.

Acknowledgements

First, I would like to thank my supervisors Sunniva Siem and Magne Guttormsen for their support and helpful answers. This thesis work was conducted during the COVID-19 pandemic¹, and I appreciate your efforts to give me good guidance in these conditions. Sunniva, you are always positive and encouraging and you have given me a lot of good feedback during the writing process. Thanks for everything you do for the students. The summer school in South Africa was memorable, and it's a shame we did not get to do another one. Magne, you have always been quick to answer my e-mails and available for short notice discussions on Zoom. When I started my master's degree I was a novice within nuclear physics and your patience and good explanations have been indispensable.

Thanks to Julian E. Vevik, for a good collaboration when calibrating our experimental data. It has been nice sharing an office with you the last two years, good luck with your thesis!

Thanks to Fabio Zeiser, for setting aside time while writing his Ph.D. thesis to answer my questions about the OMpy software. Our little climbing trip to Waterval Boven after the summer school, where it rained every day except the morning we left, was an experience in the Type-II fun-category².

Thanks to everyone at the 4th-floor office and the rest of the nuclear physics group at UiO for creating a good work environment during this pandemic, to Corporated INC. on the 11th-floor for getting me through my bachelor's degree, and to Lille Frøen Buldre Klub for providing convenient training facilities to keep my fingers strong during my master's degree work.

Thanks to my high school teachers Bjørn Pran and Mr. Wittkamper for sparking the nature science flame inside me.

Thanks to my supportive family for always pretending to understand when I talk about my thesis and for all the love you show me.

Last, but not least, a big thank you to my amazing girlfriend Inga. You are always supportive and help me view things from other perspectives when I have lost faith in my work.

¹I want to give a tiny thank you to the pandemic for keeping distractions at a minimum while I was working on my thesis. Again, a very tiny thank you.

²Type-I fun: Fun while it's happening. Type-II fun: Miserable while it's happening, fun to look back at. Type-III fun: miserable when it's happening and miserable to look back at.

Acronyms

γ SF	- Gamma-ray Strength Function
NLD	- Nuclear Level Density
GDR	- Giant Dipole Resonance
PDR	- Pygmy Dipole Resonance
SFR	- Spin Flip Resonance
SR	- Scissors Resonance
OCL	- Oslo Cyclotron Laboratory
CACTUS	- Gamma-ray Detector Setup at OCL (pre. 2017)
SiRi	- Silicon Ring particle detector
OMPy	- Oslo Method python
OMS	- Oslo Method Software
BSFG	- Back Shifted Fermi Gas model
CT	- Constant Temperature model

Contents

List of Figures	ix
List of Tables	xv
1 Introduction	1
1.1 Astrophysical nucleosynthesis and the r-process	2
1.2 Thorium Reactors	3
1.3 Further motivation - the new Oslo method software OMpy	4
2 Average nuclear properties in the quasicontinuum	7
2.1 Nuclear Level Density	7
2.2 γ -Ray Strength Function	9
2.3 Resonances	10
3 Experimental Setup and Data Calibration	13
3.1 Oslo Cyclotron Laboratory (OCL)	13
3.2 CACTUS detector setup	15
3.3 Detector calibration	17
3.3.1 SiRi particle detector calibration	19
3.3.2 NaI gamma-ray detector calibration	19
3.3.3 Time calibration	20
3.3.4 Additional adjustments	23
4 Data Analysis	27
4.1 Oslo Method	27
4.1.1 Unfolding the (E_γ, E_x) coincidence matrix	27
4.1.2 Obtaining the First Generation Matrix γ -ray spectra .	29
4.1.3 Extracting the NLD and γ SF	31
4.1.4 Normalizing the NLD and γ SF	33
4.2 Implementation - OMpy	33
5 Results and discussion	37
5.1 γ SF and NLD	37
5.2 Scissors Resonance	41
5.3 Discussion	51

5.3.1	NLD and γ SF from the OMpy software	51
5.3.2	Scissors Resonance	52
5.4	Concluding Remarks	52
5.5	Outlooks	53
A	Boundaries on the normalization parameter α	55
B	Tables and figures for the more constrained fit with the 185 keV/bin dispersion	61
	Bibliography	65

List of Figures

3.6	Projections of all the γ -ray detectors. Left panel: the experimental data sorted with a gate on the $^{208}\text{Pb}(\alpha, t'\gamma)^{209}\text{Bi}$ reaction. (Peak A) points at the 0.89 MeV peak. Right panel: the experimental data sorted with a gate on the $^{208}\text{Pb}(\alpha, \alpha'\gamma)^{208}\text{Pb}$ reaction (Peak B) points at the 2.6 MeV peak (see text).	20
3.7	Upper panel: plots of the γ -ray spectra for all detectors from the ^{208}Pb run after the calibration. Lower panel: Projection of upper panel down on the $E(\text{NaI})$ axis. The red arrow shows where (Peak B) from Fig. 3.6 ended up after the linear calibration. The γ -ray annihilation peak at 0.511 MeV is also visible. (Peak A) from Fig. 3.6 is not visible in this ungated plot, but was observed with gate requirements.	21
3.8	Upper panel: plots of the γ -ray spectra for all detectors from the ^{233}U run. The 4.4 MeV peak from the ^{12}C contamination and its apparent Doppler shift is visible. Lower panel: The $E(\text{NaI})$ counts are projected to the horizontal axis, where the 4.4 MeV and 0.511 MeV peaks are visible.	22
3.9	The time vs. energy spectrum in the upper panel and the projection on the time axis in the lower panel. Red dashed lines enclose the true coincidence peak, while red dotted lines enclose the peak used for background subtraction.	23
3.10	Upper panel: The raw (E_γ, E_x) coincidence-matrix. The lower dashed line is the $E_x = E_\gamma$ diagonal from the first calibration attempt, while the upper dotted line is what seems to be the true diagonal (see text). Lower panel: The (E_γ, E_x) coincidence matrix gated on fission reactions and projected on to the excitation energy axis. The theoretical inner $B_{F,i}$ and outer $B_{F,o}$ fission barrier from RIPL-3 [11] are marked with red arrows.	25
3.11	Upper panel: The raw (E_γ, E_x) coincidence matrix after the diagonal calibration. The true $E_x = E_\gamma$ diagonal is plotted with a red dashed line. Lower panel: The (E_γ, E_x) coincidence matrix gated on fission reactions and projected on to the excitation energy axis. The inner and outer fission barriers, marked with red arrows, correlates with previous findings (see text).	26
4.1	The response matrix of the CACTUS detector setup obtained in Ref. [36, 37]. The incoming γ -ray energy is plotted on the y-axis and the measured γ -ray energy is plotted on the x-axis.	28

4.2	From left: the raw, unfolded and first generation matrices. The first generation matrix has been rebinned to 120 keV per bin and the red, stippled trapezoid marks the area where the NLD and γ SF are extracted from, with $E_{x,min} = 3.1$ MeV, $E_{x,max} = 5.1$ MeV and $E_{\gamma,min} = 1.0$ MeV.	31
4.3	Blue triangles shows data from the first generation matrix. The orange line is the product of the extracted ρ and \mathcal{T} . Each plot is gated on a certain excitation energy bin, and shows the number of counts and correlating E_γ for the given excitation energy.	32
5.1	The γ SF and NLD from OMS in blue triangles and OMpy in orange circles with dispersion of 120 keV/bin for both E_x and E_γ . The OMpy results are presented with a 68% confidence interval marked with a dark gray band. The upper panel shows the NLD, with the known discrete levels from Ref. [11] as a red, solid line and $\rho(S_n)$ as a green square. The lower panel shows the γ SF. In both panels, the OMpy extrapolation are showed as red, stippled lines and their respective extrapolation areas are marked with light gray.	38
5.2	The γ SF and NLD from OMS in blue triangles and OMpy in orange circles with dispersion of 185 keV/bin for both E_x and E_γ . The OMpy results are presented with a 68% confidence interval marked with a dark gray band. The upper panel shows the NLD, with the known discrete levels from Ref. [11] as a red, solid line and $\rho(S_n)$ as a green square. The lower panel shows the γ SF. In both panels, the OMpy extrapolation are showed as red, stippled lines and their respective extrapolation areas are marked with light gray.	40
5.3	Upper panel: The red stippled lines show the fit of the two GDR peaks and the black solid line shows the total fit. The orange circles show the γ SF from this work with a dispersion of 120 keV/bin and its uncertainty as the dark gray 68% confidence interval. The green squares are the cross-section data from Ref. [45] converted to γ SF by Eq. (2.14). The light gray area encloses the energy interval in which the GDR peaks were fit. Lower panel: Blue solid line shows the total GDR fit. The red points were used in the GDR fit.	42

5.4	Upper panel: Solid line shows the total GDR+PDR+SFR fit. A blue dotted line shows the PDR fit and a grey stippled dotted line shows the SFR fit. The orange circles show the γ SF from this work with a dispersion of 120 keV/bin and its uncertainty as the dark gray 68% confidence interval. The pink and green triangles taken from RIPL-2 data were not used as points in the fit but correlates well with the fit and the data. Lower panel: The blue solid line shows the PDR+SFR fit. The red points are a combination of the γ SF from this work and the data from Ref. [45] used to fit the PDR and SFR.	43
5.5	Upper panel: Black solid line shows the total GDR+PDR+SFR+SR fit and in the blue solid line the SR fit is excluded. Lower panel: The red area enclose the integration area used to find the strength of the SR. Black dotted lines show the upper and lower integration areas used to find the uncertainty of the SR strength. Orange circles shows the median γ SF from OMpy with a 120 keV/bin dispersion after the GDR+PDR+SFR tail was subtracted. Note that the fit of the SR is plotted as a red dashed line in the upper and lower panel, but it is not used in further analysis.	45
5.6	Input values to the fit are plotted with blue circles and the resulting values are plotted with red triangles. Upper blue line and lower green line shows the maximum and minimum allowed parameter value in the fitting procedure. The peak centroid parameters ω_{PDR} , ω_{SFR} , $\omega_{SR,1}$ and $\omega_{SR,2}$ were somewhat constrained inside relevant energy intervals and the rest of the parameters has more or less no constraints.	46
5.7	The full, less constrained fit of the GDR+PDR+SFR tail is marked with the solid purple line, and the GDR+PDR+SFR+SR fit is marked with the black solid line. The individual fits are all marked with dashed lines.	47
5.8	The resulting SR mode with the less constrained fit and a 120 keV/bin dispersion is shown as a red stippled line. The red area enclose the integration area used to find the strength of the SR. Black dashed lines show the upper and lower integration areas used to find the uncertainty of the SR strength. Orange circles shows the median γ SF from OMpy with a 120 keV/bin dispersion after the GDR+PDR+SFR tail was subtracted.	48
5.9	Comparison between the three methods described to measure the SR mode. The less constrained fit is presented with a red triangle. The two other methods are presented with a blue circle (185 keV/bin) and a green star (120 keV/bin). The upper panel shows the $B_{SR}(M1)$ strengths and the lower panel shows the ω_{SR} centroids.	49

- 5.10 Comparison of the SR from this work with previous data from
 Refs. [47, 50–52]. The B_{SR} (M1) strength are presented in the
 upper panel and ω_{SR} centroid in the lower panel. The previous
 data are all marked with green, where equivalent markers
 represent elements with equivalent proton numbers. Results
 from the three methods in the presented work is marked with
 red upward-pointing triangles. The uncertainty from this work
 comes from integrating the lower/upper boundaries of the γ SF. 50
- A.1 OMpy normalization of one of the ensemble members that
 produced unreasonable normalization results. The left panel
 shows the NLD and the right panel shows the γ SF. The
 discrete energy levels are marked with a black solid line and
 $\rho(S_n)$ with a black square in the left panel. The NLD and
 γ SF are marked with blue dots and lines. The resulting
 extrapolations are marked with green, stippled lines and the
 extrapolation areas with light gray. 56
- A.2 OMpy normalizations of the median ensemble member in
 orange, and a 68% confidence interval in light blue. The left
 panel shows the NLD and the right panel shows the γ SF. The
 discrete energy levels are marked with a black solid line and
 $\rho(S_n)$ with a black square in the left panel. The NLD and
 γ SF extrapolations are marked with green, stippled lines for a
 random selection of ensemble members and the extrapolation
 areas with light gray. 56
- A.3 These plots are generated from the same ensemble member as
 Fig. A.1. Row (a) shows the five different normalization para-
 meters and their associated probability distributions. Rows
 (b) to (e) show the covariance between the different normal-
 ization parameters. Double humped probability functions can
 be seen for all the normalization parameters. Also, all the co-
 varinces show two different solutions to the normalization for
 all parameters. The double humped probability function of
 the normalization parameter B is hard to distinguish in row
 (a), but the covariance between B and the other parameters
 indicates that B also has a double humped probability function. 57
- A.4 The probability distribution of α in the left panel and the
 covariance between α and A i the right panel, from Fig. A.3.
 The plots are generated from the same ensemble member as
 Fig. A.1. The double humped probability distribution of α is
 obvious. The covariance between the A and α parameters is
 shown in the right panel, indicating two different solutions to
 the normalization. 58

A.5	These plots are generated from the same ensemble member as as Fig. A.1 after the boundary was set on α . Row (a) shows the five different normalization parameters and their associated probability distributions. Rows (b) to (e) show the covariance between the different normalization parameters. In contrast to Fig. A.3, only one solution is found for this normalization.	59
A.6	The probability distribution of α in the left panel and the covariance between α and A in the right panel, from Fig. A.5. The plots are generated from the same ensemble member as Fig. A.1, after the boundary was set on the α parameter.	60
B.1	Upper panel: The red stippled lines show the fit of the two GDR peaks and the black solid line shows the total fit for the 185 keV/bin dispersion. The orange circles show the γ SF from this work with a dispersion of 185 keV/bin and its uncertainty as the dark gray 68% confidence interval. The green squares are the cross-section data from Ref. [45] converted to γ SF by Eq. (2.14). The light gray area encloses the energy interval in which the GDR peaks were fit. Lower panel: Blue solid line shows the total GDR fit. The red points are the points used in the GDR fit.	62
B.2	Upper panel: Solid line shows the total GDR+PDR+SFR fit for the 185 keV/bin dispersion. A blue dotted line shows the PDR fit and a grey stippled dotted line shows the SFR fit. The orange circles show the γ SF from this work with a dispersion of 185 keV/bin and its uncertainty as the dark gray 68% confidence interval. The pink and green triangles taken from RIPL-2 data were not used as points in the fit but correlates well with the fit and the data. Lower panel: The blue solid line shows the PDR+SFR fit. The red points are a combination of the γ SF from this work and the data from Ref. [45] used to fit the PDR and SFR.	63
B.3	Upper panel: Black solid line shows the total GDR+PDR+SFR+SR fit for the 185 keV/bin dispersion and in the blue solid line the SR fit is excluded. Lower panel: The red area enclose the integration area used to find the strength of the SR. Black dashed lines show the upper and lower integration areas used to find the uncertainty of the SR strength. Orange circles shows the median γ SF from OMpy with a 185 keV/bin dispersion after the GDR+PDR+SFR tail was subtracted. Note that the fit of the SR is plotted in the upper and lower panel, but it is not used in further analysis.	64

List of Tables

3.1 Available beams at the OCL	13
4.1 Parameters used in the Oslo method normalization and extraction. D_0 was taken from Ref. [11]. E_0 was taken from Ref. [40]. $\langle \Gamma_\gamma \rangle$ is the average value of nearby nuclei from Ref. [11]. The range of the temperature parameter T was chosen from previous Oslo method analysis. For the OMS implementation, the temperature parameter was set to $T = 0.39$ MeV.	34
5.1 Giant Dipole, Pygmy and Spinflip resonance parameters from the more constrained fit with a 120 keV/bin dispersion. ω , σ and Γ represents the centroid, cross section and FWHM of the given resonance peak. For the GDR, the temperature parameter was fixed at $T_f=0.2$ MeV. See text for more information about the PDR and SFR parameters.	44
5.2 The resulting Giant Dipole, Pygmy and Spinflip resonance parameters for the less constrained fit with a 120 keV/bin dispersion. ω , σ and Γ represents the centroid, cross section and FWHM of the given resonance peak. For the GDR fit, the temperature parameter arrived at $T_f = 0.23(102)$ MeV with a large uncertainty. Note the missing uncertainties, which are discussed in the text.	47
5.3 The scissors resonance parameters of ^{233}U . The resonance parameters ω_{SR} and $B_{SR}(\text{M1})$ are the centroid and strength of the resonance. The uncertainty of the strength is represented as a range. The integral range is also presented.	49
B.1 Giant Dipole, Pygmy and Spinflip resonance parameters for the 185 keV/bin dispersion less constrained results. ω , σ and Γ represents the centroid, cross section and FWHM of the given resonance peak. For the GDR fit, the temperature parameter was fixed at $T_f = 0.2$ MeV.	61

Chapter 1

Introduction

Nuclear physics is the study of the interaction between neutrons and protons inside the core of the atom. Light nuclei such as hydrogen and helium can be relatively precisely explained by known theoretical models. But the chart of nuclei is big (see Fig. 1.1), and stretches all the way from nuclei like helium-4 with 2 neutrons and 2 protons interacting, to heavier nuclei like Uranium-233 with 141 neutrons and 92 protons interacting! Needless to say, different theoretical models and experimental approaches need to be utilized to understand the interaction between and properties of nuclei across the chart.

Nuclei are often described and identified by their energy levels. A nucleus in an excited state below the neutron separation energy S_n , will decay to a lower energy level by emitting a γ -ray. At low excitation energies, labelled the discrete energy region, these levels are relatively easy to distinguish between. Experiments with γ -spectroscopy can be used to make out the different levels. Each energy level can then be assigned a certain γ -ray transition rate, which tells us the probability of γ -decay from the given level with a certain γ -energy. If the nuclei are excited to higher energies, typically above 10 MeV, the energy levels will overlap so they can not be separated from each other. This region is often called the continuum region. Nuclei that are excited above the discrete region, but below the continuum-region, are in the quasi-continuum region. Here, the energy levels do not overlap, but they are so close that it is no point in trying to separate them from each other. Instead, energy levels and γ -ray transition rates are represented by statistical properties, known as nuclear level densities (NLD) and γ -ray strength functions (γ SF). In this work, the NLD and γ SF are found for the ^{233}U nucleus. Several experimental methods can extract either the NLD or γ SF. In this work, the Oslo method is utilized which uniquely extracts the NLD and γ SF simultaneously from the same experimental data.

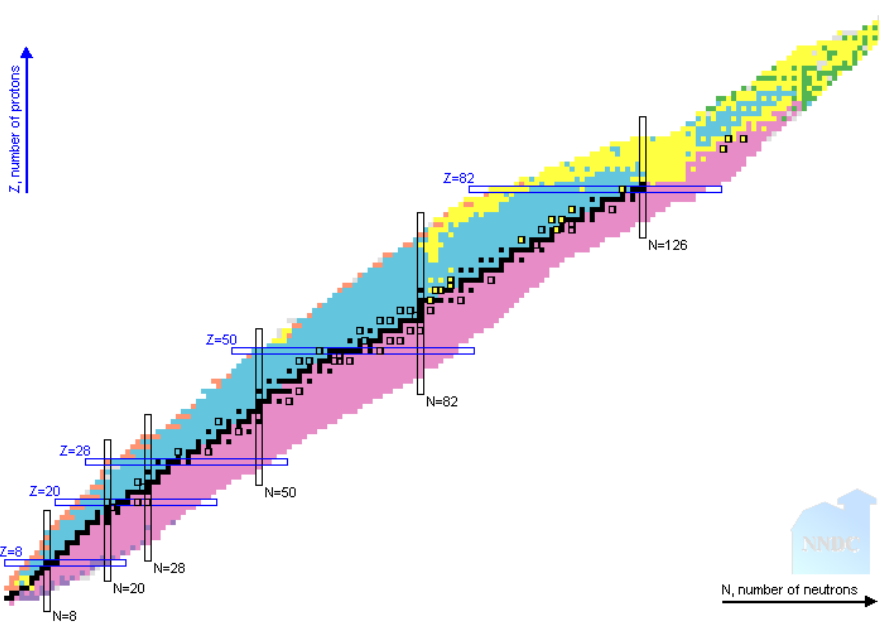


Figure 1.1: *The chart of nuclei from Ref. [1]. Different colors represent the decay-mode of the given nucleus, where the three main ones are pink= β^- , blue= β^+ and yellow= α decay. The magic nuclear numbers 8, 20, 28, 50, 82 and 126 are highlighted and characterize single-particle energy gaps.*

In some theoretical models, a sum of different resonances is used to describe the γ SF. This work focus on the scissors resonance (SR), which is a significant part of the γ SF for deformed nuclei like ^{233}U . The SR and its peak-parameters can be input in relevant theoretical models to test their performance and help improve them. Historically, the SR is represented in part by its centroid ω_{SR} and its reduced transition probability $B_{SR}(\text{M1})$, referred to as its strength. The SR from this analysis adds itself to the range of previous actinide SR's observed with the Oslo method analysis, and results from this work are compared to these former findings.

Radiative neutron capture cross-sections are prominent for many areas of nuclear physics, particularly reactor physics and nuclear astrophysics. The NLD and γ SF found in this work can be used as input in existing nuclear reaction codes to calculate these cross-sections.

1.1 Astrophysical nucleosynthesis and the r-process

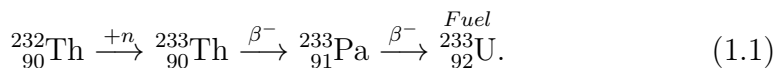
Nucleosynthesis is the creation process of nuclei. One of the main contributors to the production of all elements is the neutron capture process. Nuclei lighter than iron (proton number $Z < 26$) are made from charged particle reactions in stellar burning. Two of the other main contributors

of nucleosynthesis are the radiative neutron and proton capture processes, where nuclei undergo the (n,γ) or (p,γ) reaction. These processes are responsible for all the known elements heavier than iron. Usually, the neutron capture processes are categorized into the slow (s) and rapid (r) processes (and sometimes the intermediate (i) process between the s and r). The s-process occur for nuclei close to the valley of stability, alternating between neutron capture and β -decay. This process is responsible for the existence of elements lighter than lead ($Z < 82$). The r-process produces the most neutron-rich nuclei far from the valley of stability. Simply put, the r-process happens in the following way: A nucleus will rapidly capture neutrons (hence the name) until it is so neutron-rich that the cross-section for capturing more neutrons is lower than the β -decay cross-section within its current environment. The nucleus has reached a so-called branching point and proceeds to β -decay where a neutron is turned into a proton and the nucleus becomes a new element. This new element can either continue to β -decay, or it can capture more neutrons, depending on its cross-sections and the current environment.

There is still much unknown about the r-process, which can only happen in very high-temperature, neutron-rich environments. Until recently, the occurrence of these neutron-rich environments had not been established. Different astrophysical phenomenons had been suggested, but the discovery of a neutron star merger in 2017 and the detection of its resulting electromagnetic radiation confirmed the r-process' existence in Ref. [2]. To understand more about the r-process and astrophysical nucleosynthesis, large-scale simulations can be performed. A large part of these simulations is the neutron capture cross-sections where one of the main ingredients is the NLD and γ SF for relevant nuclei in the r-process.

1.2 Thorium Reactors

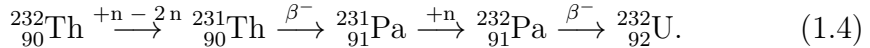
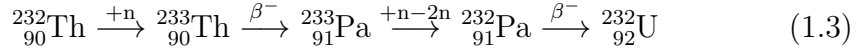
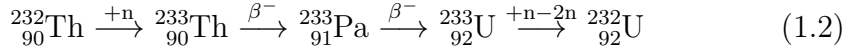
In recent years, nuclear energy using thorium as fuel has gained public attention. With the aspiration of generating less nuclear waste and being ineligible for making nuclear weapons, it may have sparked a promising future for nuclear energy and its public opinion. While thorium is getting all the fame, it is another element that produce all the energy. When thorium is found in nature it consists mostly of the ^{232}Th isotope. The thorium fuel follows the cycle given by



This process is initiated by a neutron and ^{232}Th goes through a transformation process from ^{233}Th through ^{233}Pa . The final stop in this fuel cycle is ^{233}U , which is the isotope that actually undergoes fission!

While promising a rose garden, there are drawbacks to the thorium fuel cycle. In burning thorium there are three processes, initiated by high energy

neutrons and the (n,2n) reaction, that will produce the unwanted ^{232}U isotope by the following cycles



With its relatively short half-life of approximately 69 years, and its decay to strong γ -ray emitters, ^{232}U makes spent thorium fuel hard to handle. Needless to say, the desire for ^{232}U to capture a neutron, turn into ^{233}U , and fission is high. Most previous experiments with heavy nuclei rely on the neutron capture reaction. Since ^{232}U is hard to handle, few, if any, neutron capture experiments have been done with this nucleus. As mentioned in Sec. 1.1, the NLD and γ SF found in this thesis can be used as input in cross-section calculations for the $^{232}\text{U}(n,\gamma)$ reaction. These cross-sections can be used in advanced nuclear reactor simulations to help make the best reactor environments to minimize the amount of ^{232}U in the spent Thorium fuel.

1.3 Further motivation - the new Oslo method software OMpy

The Oslo method has been developed by the nuclear physics group at the University of Oslo for the past 38 years [3–6]. Since first introduced, it is the only known method that simultaneously extract the NLD and γ SF from the same experimental data. The Oslo Cyclotron Laboratory (OCL) and its detector setup have been built to specialize in extracting data for this method. Since 2000, the Oslo method analysis has been performed with the Oslo method software (OMS), developed by Guttormsen, Schiller et al. [7]. Over the years there have been several efforts of strengthening the Oslo method by improving its uncertainty estimation. Dr. A. C. Larsen et al. published a paper in 2011 [8], laying out the possible systematic errors of the whole Oslo method. Motivated in part by this paper, a new Oslo method software has been developed in which several of the methods of uncertainty estimation has been reviewed and improved. While the standard OMS is written in Fortran and C, the new software is written in Python with “modularity in mind”. Named OMpy (Oslo method Python) [9], it uses modern software development strategies and enables the user to be more involved in the analysis process. For example, with the class structure of the software, the user can easily change the current unfolding procedure to test future unfolding procedures. This work presents the first Oslo method

analysis with the new OMpy software, except the data presented in the OMpy article [9].

This thesis is organized in the following way: Chapter 2 includes relevant theoretical background for the NLD, γ SF, and dipole resonances. Chapter 3 introduces the conducted experiment and data preparation for this work. Chapter 4 is devoted to the data analysis, namely the Oslo method. This chapter also includes an introduction to OMpy and a selection of its implemented methods. The results are presented and discussed in Chapter 5, along with concluding remarks and outlooks. Appendix A is included to justify boundaries set on the OMpy normalization parameters. Appendix B contains additional plots related to the scissors resonance investigation.

Chapter 2

Average nuclear properties in the quasicontinuum

The excitation energy regime of a nucleus can be divided into three regions. For this classification, the level-spacing D and the width of the states Γ is used. In the low, discrete energy region, the levels can easily be separated from each other by the relation

$$\Gamma \ll D. \quad (2.1)$$

As the excitation energy increases, the level-spacing D decrease. Furthermore, the width Γ will increase with increasing energy. In the high energy continuum region, the energy levels overlap and can not be separated. D and Γ are then related by

$$\Gamma \geq D. \quad (2.2)$$

In the quasi-continuum, the levels do not overlap, but they are so close that they are practically indistinguishable. D and Γ are then related by

$$\Gamma \leq D. \quad (2.3)$$

In the quasi-continuum region, the energy levels are usually described with average properties. The average quantities NLD and γ SF, relevant for this work, replace the concepts of discrete energy levels and their individual transition rates.

2.1 Nuclear Level Density

The nuclear level density of a nucleus with excitation energy E_x is defined as the number of quantum energy levels per unit excitation energy, given by

$$\rho(E_x) = \frac{\Delta N}{\Delta E} = \frac{1}{D}, \quad (2.4)$$

where ΔN is the number of levels found within the excitation energy bin ΔE at E_x and D is the average level spacing.

Several models have been used to represent the NLD. Up to excitation energies of 10 MeV, the NLD is usually described with the *Constant-Temperature model* (CT). In Ref. [10], it was found that the number of levels per excitation energy followed the relation

$$N(E_x) = \exp\left(\frac{E_x - E_0}{T}\right), \quad (2.5)$$

where T corresponds to an assumed constant nuclear temperature and E_0 is the energy shift parameter. The total level density can then be written by combining Eqs. (2.4-2.5) to get the relation [11, 12]

$$\rho(E_x) = \frac{dN(E_x)}{dE} = \frac{1}{T} \exp\left(\frac{E_x - E_0}{T}\right). \quad (2.6)$$

With this definition the NLD only depends on the excitation energy E_x of the nucleus. In reality, it should also depend on the spin J and parity π , leading to a factorization of ρ by

$$\rho(E_x, J, \pi) = \rho(E_x)g(E_x, J, \pi), \quad (2.7)$$

where $g(E_x, J, \pi)$ is the *spin-parity distribution*. When extracting the NLD using the Oslo method, one only extracts the $\rho(E_x)$ part of the NLD. To get the full factorization of ρ , one assumes an equal number of levels for each parity, which gives

$$\rho(E_x, J, \pi) \approx \frac{1}{2}\rho(E_x, J), \quad (2.8)$$

for higher energies. Following this, one needs to find the spin distribution $g(E_x, J)$. A common practice is to use the Ericson spin distribution from Ref. [13], given by

$$g(E_x, J) = \exp \frac{-J^2}{2\sigma^2(E_x)} - \exp \frac{-(J+1)^2}{2\sigma^2(E_x)} \approx \frac{2J+1}{2\sigma^2(E_x)} \exp \frac{-(J+1/2)^2}{2\sigma^2(E_x)}, \quad (2.9)$$

where $\sigma(E_x)$ is the *spin-cutoff parameter*. There are several models which can be used to describe $\sigma(E_x)$, which may lead to uncertainties in the normalization of the NLD and γ SF. In this work, the Back Shifted Fermi Gas model (BSFG) from Ref. [14] was used to describe $\sigma(E_x)$. Using the BSFG model and combining Eqs. (2.8-2.9), the NLD can be written as

$$\rho(E_x) = \frac{\exp[2\sqrt{a(E_x - E_1)}]}{12\sqrt{2}\sigma^2(E_x)a^{1/4}(E_x - E_1)^{5/4}}, \quad (2.10)$$

where a is the level density parameter, E_1 is the backshift parameter and $\sigma^2(E_x)$ is given by

$$\sigma^2(E_x) = 0.014A^{2/3} \frac{1 + \sqrt{4a(E_x - E_1)}}{2a}, \quad (2.11)$$

where A is the mass number of the nucleus.

2.2 γ -Ray Strength Function

For excitation energies below the particle separation energy, the nucleus will mainly decay by γ -ray emission, though in some rare cases with conversion electrons or electron-positron pairs. The γ SF describes the probability that a nuclei will decay between two levels by emitting γ -rays. For a multipolarity XL of γ -radiation, the γ SF can be written as [12, 15]

$$f_{XL}(E_\gamma, E_i, J_i, \pi_i) = \frac{\langle \Gamma_\gamma^{XL} \rangle(E_\gamma, E_i, J_i, \pi_i)}{E_\gamma^{2L+1}} \rho(E_i, J_i, \pi_i), \quad (2.12)$$

where $\langle \Gamma_\gamma^{XL} \rangle(E_\gamma, E_i, J_i, \pi_i)$ is the average partial decay width for an excitation energy E_i with spin J_i and parity π_i , with a γ decay energy of E_γ and multipolarity XL . A γ -decay can be either magnetic ($X = M$) or electric ($X = E$). In the Oslo method, one assumes that dipole radiation dominates the relevant excitation energies, hence $L = 1$. Notice that Eq. (2.12) depends on the full factorization of ρ as mentioned in Sec. 2.1.

The strength function can be related to the transmission coefficient \mathcal{T} as [16]

$$\mathcal{T}_{XL}(E_\gamma) = 2\pi E_\gamma^{2L+1} f_{XL}(E_\gamma). \quad (2.13)$$

The transmission coefficient \mathcal{T} can be extracted experimentally with the Oslo method, leaving Eq. (2.13) indispensable for this work.

Another useful relation is [16]

$$\vec{f}_{XL} = \frac{1}{(2L+1)\pi^2 \hbar^2 c^2} \frac{\sigma_{XL}}{E_\gamma^{2L-2}}, \quad (2.14)$$

where the strength function \vec{f}_{XL} is related to the photo absorption cross section σ_{XL} . This relation is used to convert previous experimental σ_{XL} into strength functions, for comparing with the obtained strength function in this work.

In the Oslo method, the γ SF and NLD are simultaneously extracted from the same (E_γ, E_x) coincidence matrix (sometimes referred to as the particle- γ coincidence matrix). This extraction relies on Fermi's golden rule, given by [17]

$$\lambda = \frac{2\pi}{\hbar} |\langle f | \hat{H} | i \rangle|^2 \rho(E_f), \quad (2.15)$$

which states the transition probability λ from an initial state i to a final state f can be expressed by a product of the level density of the final state $\rho(E_f)$ and a small perturbation Hamiltonian \hat{H} between the two states. The experimental (E_γ, E_x) coincidence matrix is related to λ when performing the extraction. The transmission coefficient \mathcal{T} , converted to the γ SF by Eq. (2.13) in a later stage of the analysis, can then be related to $|\langle f | \hat{H} | i \rangle|^2$ in Eq. (2.15). For this relation to be true, one need to use the generalized Brink-Axel (gBA) hypothesis [18, 19]. Usually, one distinguishes between the

upward (f_{\uparrow}) and downward (f_{\downarrow}) strength, or the γ -absorption and γ -decay. The gBA results in a strength function that is independent of the upward or downward strength. In addition, the gBA can be used to exclude the spin J and parity π dependency of the strength function. Including the \uparrow/\downarrow dependency in Eq. (2.12), the hypothesis results in a strength function that is independent of excitation energy, spin and parity and only dependent on the E_{γ} energy given by

$$f_{\uparrow/\downarrow}(E_{\gamma}, E_i, J_i, \pi_i) \approx f_{XL}(E_{\gamma}). \quad (2.16)$$

Because of experimental constraints, the NLD is extracted with no spin or parity information. This, together with the validity of the extraction by Fermi's golden rule, leaves the gBA hypothesis indispensable for the Oslo method analysis.

2.3 Resonances

The general shape of the strength function for a nucleus can be described by different resonances as illustrated in Fig. 2.1. For all nuclei, the strength function is dominated by the E1 Giant Dipole Resonance (GDR). In lower E_{γ} energy regions other resonances are more or less present in different nuclei.

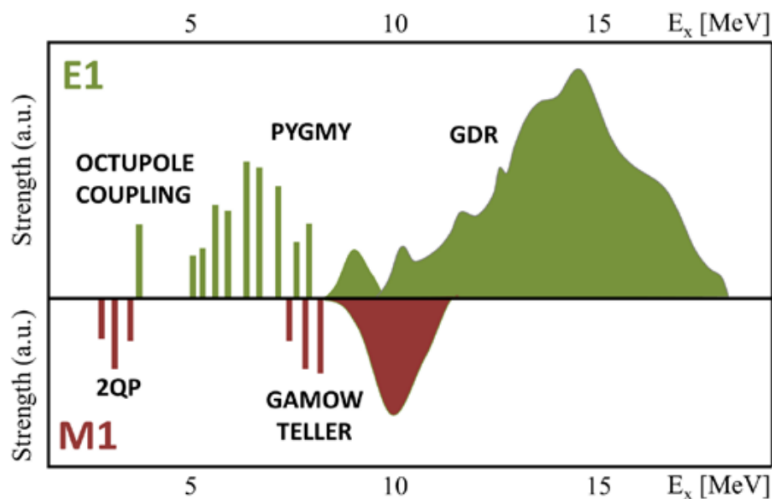


Figure 2.1: Illustrations of the general shape of the dipole strength in atomic nuclei, from Ref. [20]. Note that this figure shows the $f(E_x)$ strength with resonances built only on the ground state energy where $E_x = E_{\gamma}$. In this work the $f(E_{\gamma})$ is investigated, which includes resonances in higher-lying energy regions.

A resonance in the γ SF is an E_{γ} energy interval where the nucleus prefers to decay. Historically, most of the resonances studied in this work have been

explained with macroscopic models of nuclei as illustrated in Fig. 2.2. In Ref. [21] it was shown that these macroscopic models can come short, and including microscopic models in the picture needs to be done to improve theoretical calculations.

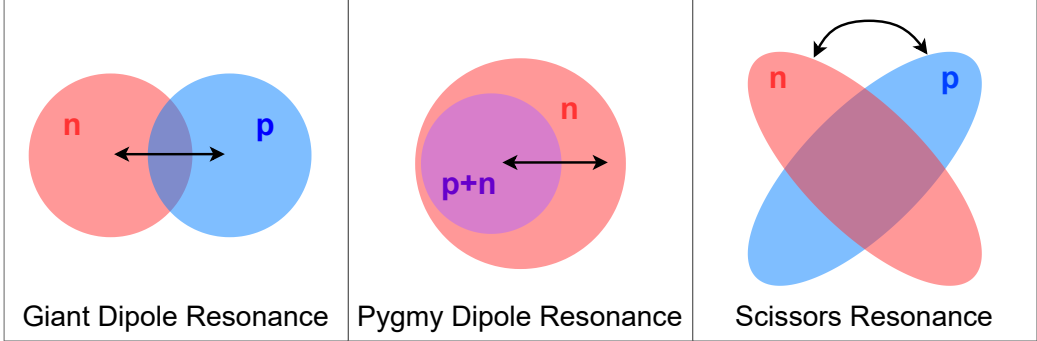


Figure 2.2: *Illustrations of the macroscopic description of the motion of neutrons (n) and protons (p) against each other for the giant dipole, pygmy and scissors resonance.*

The GDR is often described macroscopically as the collective motion of neutrons against protons in the nucleus, as illustrated in Fig. 2.2. Usually, the shape is represented by the Generalized Lorentzian function (GLo), given by.

$$f_{GLo}(E_\gamma) = \frac{\sigma_{GLo}\Gamma_{GLo}}{3\pi^2\hbar^2c^2} \left(\frac{E_\gamma\Gamma_K(E_\gamma)}{(E_\gamma^2 - \omega_{GLo}^2)^2 + E_\gamma^2\Gamma_K(E_\gamma)^2} + 0.7 \frac{\Gamma_K(E_\gamma = 0)}{\omega_{GLo}^3} \right), \quad (2.17)$$

where ω_{GLo} , σ_{GLo} and Γ_{GLo} represents the centroid, cross-section, and full width at half maximum (FWHM) of the peak. The Γ -width function is given by

$$\Gamma_K(E_\gamma) = \frac{\Gamma_{GLo}}{\omega_{GLo}^2}(E_\gamma^2 + 4\pi^2T_f^2). \quad (2.18)$$

and depends on the γ -energy E_γ and the temperature T_f . For lower E_γ there are other smaller resonances, like the E1 Pygmy Dipole Resonance (PDR) and M1 Spinflip Resonance (SFR). The PDR is often described macroscopically as the collective motion of neutrons and protons against the neutron shell in the nucleus, as illustrated in Fig. 2.2. The shapes of the lower lying resonances are usually represented by the Specialized Lorentzian function (SLo), given by

$$f_{SLo}(E_\gamma) = \frac{1}{3\pi^2\hbar^2c^2} \frac{\sigma_{SLo}E_\gamma\Gamma_{SLo}}{(E_\gamma^2 - \omega_{SLo}^2)^2 + E_\gamma^2\Gamma_{SLo}^2}, \quad (2.19)$$

with parameters comparable to the GLo³.

³Note that the ω_{GLo} and ω_{SLo} centroid parameters sometimes are denoted E_{GLo} and E_{SLo} in the literature

For some nuclei one can also find the lower-lying $M1$ Resonance, typically around 2-3 MeV [21], referred to as the Scissors Mode or the Scissors Resonance (SR) [22, 23]. The SR was first predicted theoretically in Refs. [22, 24] and later supported by experimental observations in Ref. [25]. It is historically described as a macroscopic scissor-like motion of neutrons and protons in the nucleus, as illustrated in Fig. 2.2. When the SR is investigated, its strength is usually categorized with a reduced transition probability $B(M1)$ for magnetic dipole transitions, as in Ref. [26]. One typically measure the $B(M1)$ strength by fitting the assumed scissors resonance peak in the γ SF with SLo functions in order to compare with previous data. Since the Oslo method does not distinguish between electric or magnetic transitions, enhancements in the γ SF around 2-3 MeV are usually assumed to be the SR with an $M1$ transition.

By using the GLo and SLo models to fit the GDR, PDR, and SFR to previous data, and data from this work, the SR of ^{233}U is found with a proposed centroid and strength. By integrating the γ SF after subtracting the GDR tail, one can obtain the $B_{SR}(M1)$ scissors resonance strength by the relation from Ref. [27], given by

$$B_{SR} = \int \frac{dB_{SR}}{dE_\gamma} = \frac{27(\hbar c)^3}{16\pi} \int f_{SR}(E_\gamma) dE_\gamma, \quad (2.20)$$

where f_{SR} is the strength function after the subtraction of the tail. In Ref. [27] it was shown that the result relied heavily on the integration limits. In several previous analyses of the scissors resonance, one would fit the SR with one or two SLo functions and use an approximation, and the resulting resonance parameters, to find the $B_{SR}(M1)$ strength. This approximation is given by

$$B_{SR} = \frac{9\hbar c}{32\pi^2} \left(\frac{\sigma_{SR}\Gamma_{SR}}{\omega_{SR}} \right), \quad (2.21)$$

where ω_{SR} , Γ_{SR} and σ_{SR} are the centroid, width, and cross-section of the scissors resonance from the SLo fit. In Ref. [27] it was shown that this approximation resulted in a $\approx 10\%$ larger $B_{SR}(M1)$ strength than by integrating according to Eq. (2.20). The integral method is utilized to investigate the scissors resonance in this work.

Chapter 3

Experimental Setup and Data Calibration

3.1 Oslo Cyclotron Laboratory (OCL)

Since 1979, the Oslo Cyclotron Laboratory (OCL) has used a Scanditronix MC-35 cyclotron with possible beams listed in Tab. 3.1.

Table 3.1: *Available beams at the OCL*

Ion	Charge state	Energy range [MeV]	Max. cyclotron intensity [μA]
Proton	$^1\text{H}^+$	2-35	100
Deutron	$^2\text{H}^+$	4-18	100
Helium-3	$^3\text{He}^{++}$	6-47	50
Helium-4	$^4\text{He}^{++}$	8-35	50

In Fig. 3.1, the experimental hall of the OCL is shown. The beam travels through four slits and three quadrupole magnets to focus the beam. It is also bent 90° to increase the energy resolution. When the beam reaches the target, it has a diameter of 1-2 mm [28].

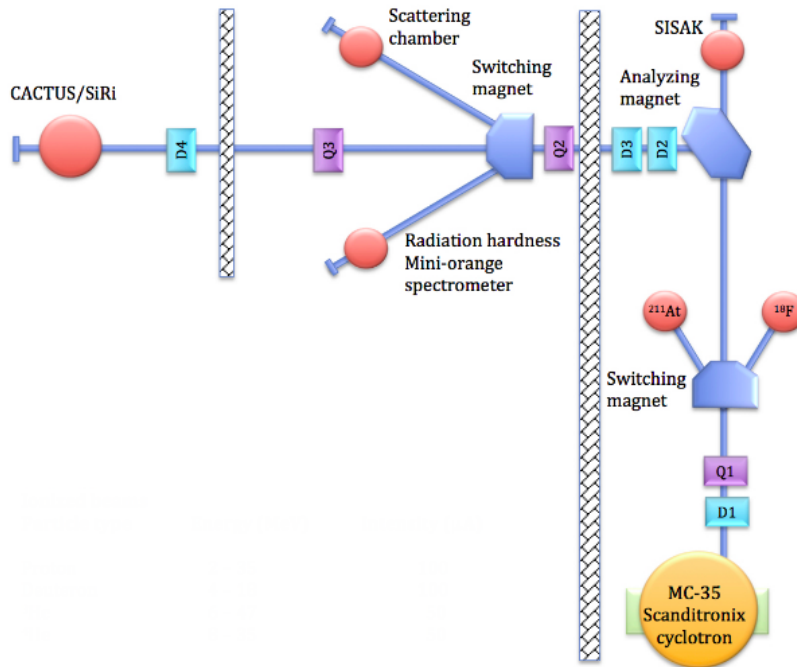


Figure 3.1: *The OCL experimental hall. The figure is adapted from Ref. [7]. Dipole magnets $D1..D4$ and the quadrupole magnets $Q1..Q3$ are all used to focus the beam.*

The experiment for this work was conducted at OCL in September/October of 2012 with the purpose of studying the ^{233}U nucleus. For the presented analysis, the desired reaction was $^{233}\text{U}(\alpha, \alpha'\gamma)$. The CACTUS detector setup was used, with a total of 26 NaI(Tl) γ -ray telescopes and 64 silicon particle telescopes. The target consisted of 0.2 mg/cm^2 ^{233}U that was deposited on to a backing of $\approx 2.3 \text{ mg/cm}^2$ ^{nat}Be [29, 30]. In the interest of detecting fission fragments for a separate analysis, the ^{233}U was facing the Nuclear Instrument for Fission Fragments detector (NIFF) as seen in the left panel of Fig. 3.2. To excite the heavy ^{233}U nucleus, a beam of 30 MeV α -particles with an intensity of 0.35-1.0 nA was used to bombard the target for about seven days.

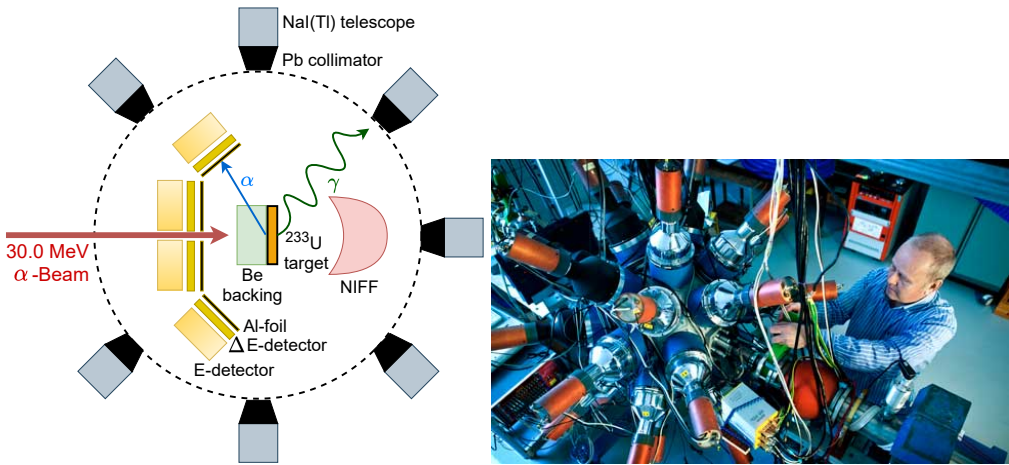


Figure 3.2: *Left panel:* illustration of the setup (not to scale). *Right panel:* the CACTUS detector, picture taken from Ref. [7].

3.2 CACTUS detector setup

The CACTUS detector setup consists of a total of 28 NaI(Tl) γ -ray scintillators (26 of which were used in this experiment) and the Silicon Ring (SiRi) particle telescope. The combined CACTUS-SiRi system is used to detect particle- γ coincidences, and designed specifically for the Oslo method analysis.

The front of the 12.7×12.7 cm NaI(Tl) crystals, were all placed on a sphere 22 cm from the target. All telescopes are lead-collimated to focus the incoming γ -rays. Taking the reduced radius due to the lead collimators into account, the telescopes cover a total solid angle of $\Omega = 14.1\%$ of the 4π sphere.

The SiRi particle telescope has a total of eight 1.55 mm thick silicon E detector pads. Each pad has 0.13 mm thick silicon ΔE detector strips in front which are separated into eight strips as illustrated in the right panel of Fig. 3.3. This adds up to a total of 64 particle telescopes. Each of the E detector pads are placed together in a ring as seen in the left panel of Fig. 3.3. Detected particles travel through the thin ΔE detector before they stop in the thicker E detector. In front of the ΔE detector, there is a $10.5 \mu\text{m}$ thick aluminum shield, with the purpose of stopping δ -electrons and fission fragments.

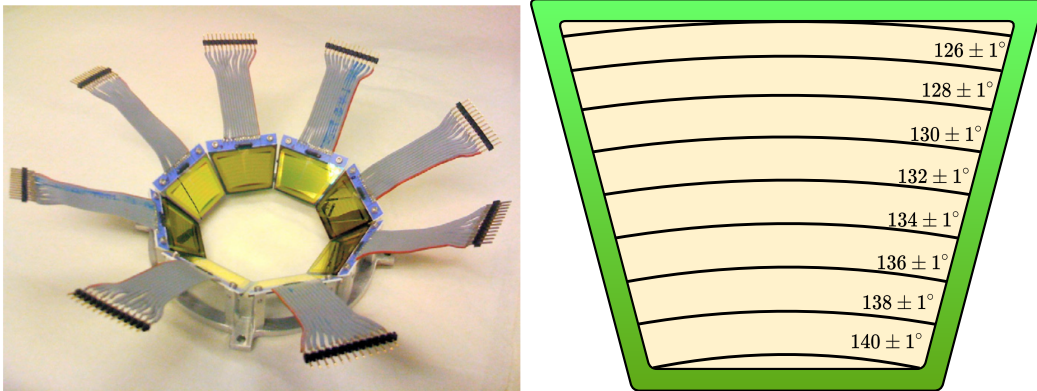


Figure 3.3: *Left panel:* the SiRi detector setup, picture taken from Ref. [31]. *Right panel:* an illustration of one of the $(E, \Delta E)$ pads (not to scale).

SiRi can be placed both in forward (40° - 54°) and backward angles (126° - 140°) [31], so one can choose to distinguish between compound reactions and other reactions. In wanting to minimize the elastic peak and be able to have a higher beam intensity, it was decided to place SiRi at backward angles for this experiment. Another effect of this is a wider and larger spin-distribution because of the transfer of angular momentum between the incoming particle and the target.

In addition, the CACTUS detector setup included an array of Parallel Plate Avalanche Counters (PPACs) for the detection of heavy-ion fission fragments, denoted NIFF [32].

To detect particle- γ coincidences, an event has to be accepted. In the electronics setup of the experiment, there are several tests performed before the signals are stored as data, to ensure the detected particles and γ -rays coincide. Acceptance of such an event is based on the following conditions [33]:

- Only one ΔE detector has fired,
- the ΔE signal exceeds a certain amplitude, corresponding to a signal from a particle with charge $Z > 1$,
- the corresponding E detector has fired,
- no other ΔE signal arrives within $\pm 4\mu s$.

Only when these requirements are fulfilled the detected coincidences are recorded to disk.

In SiRi, the detected α -particles will deposit energy in the front and back detector before stopping. Using the Bethe-Bloch formula (Eq. (3.1)), one can calculate the deposited energy in the E and ΔE detector. The Bethe-Bloch formula is given by

$$\frac{dE}{dx} = 2\pi N_a r_e^2 c^2 \rho \frac{Z}{A} \frac{z^2}{\beta} \left[\ln \left(\frac{2m_e \gamma^2 v^2 W_{max}}{I^2} - 2\beta \right) \right] \quad (3.1)$$

with variables:

N_a :	Avogadro constant	z :	charge of ionizing particle
r_e :	Electron radius	v :	speed of the particle
m_e :	Electron mass	β :	v/c
c :	Speed of light	γ :	Lorentz factor $1/\sqrt{(1 - \beta^2)}$
ρ :	Density of absorber (Si)	W_{max} :	maximum energy transfer in a collision
A :	Mass number of absorber (Si)	I :	mean excitation potential
Z :	Proton number of absorber (Si)		

Plotting the deposited energy in the E detector vs. the ΔE detector, one can see “banana”-like shapes (see Figs. 3.4 and 3.5) referred to as banana-plots in this work. Each of these “bananas” represents a certain particle through its unique $(E, \Delta E)$ relation. The banana-plots were used to gate on α particles only. This gate, together with the acceptance of a particle- γ coincidence as mentioned above, was used to calibrate the detectors to ensure the only data used in the analysis were from the desired $^{233}\text{U}(\alpha, \alpha'\gamma)$ reaction.

3.3 Detector calibration

For ^{233}U and other heavy nuclei, the density of the discrete energy levels is often high and the different levels are hard to separate. Therefore, the ^{233}U target was replaced with a ^{208}Pb target after the initial run, in the interest of calibrating the particle and γ -ray data.

Comparisons between the ^{233}U and ^{208}Pb data with reaction kinematics and Q -value calculations were done to confirm the particle calibrations. Similarly, the γ -ray calibration was verified by comparing the calibrated ^{233}U -data with known peaks in the γ -ray spectrum. The particle and γ -ray detector calibrations are presented in the following sections.

The detector calibrations use the assumption of a linear relationship between the output channel and the expected energy given by

$$E = a \cdot ch + b, \quad (3.2)$$

where E is the expected energy, ch represents the given channel number, and a and b are the gain and shift parameters, respectively. With this assumption, one can use two or more points in the detected spectra to convert the given channel number ch to known energies E by finding the values of the gain a and shift b parameters.

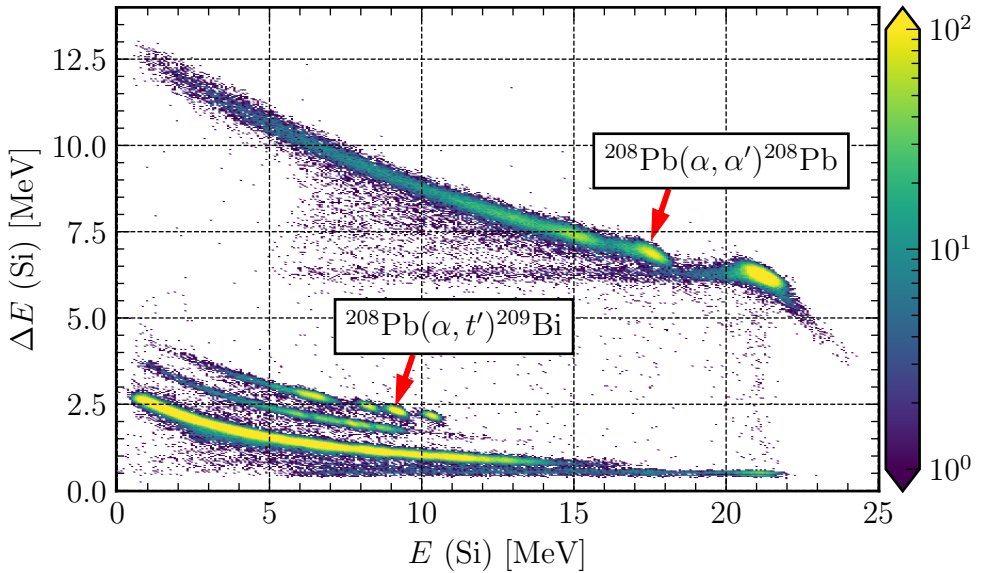


Figure 3.4: Banana-plot for all of the SiRi telescopes from the ^{208}Pb run. The peaks used for particle calibration are marked with red arrows.

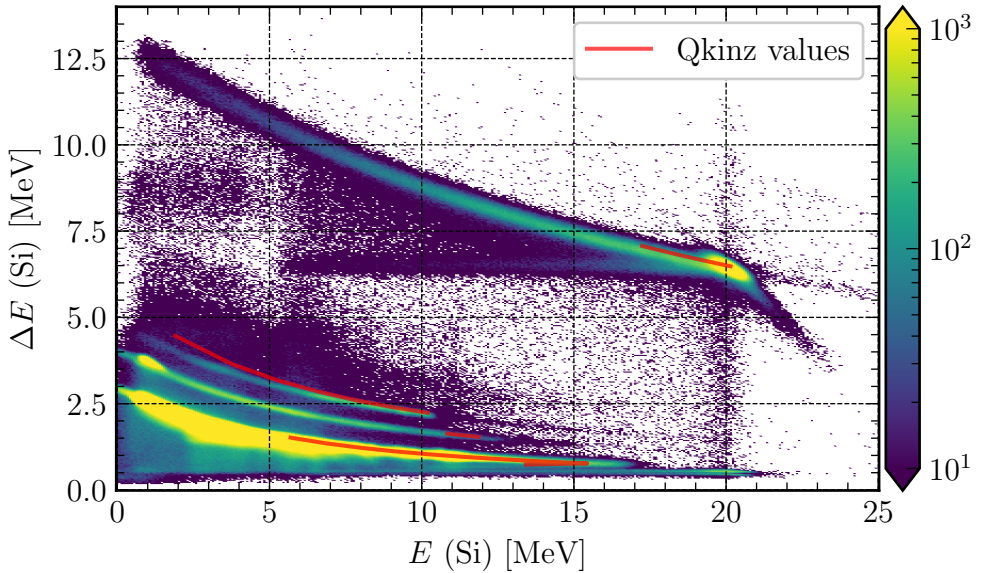


Figure 3.5: Calibrated banana-plot for the ^{233}U experiment. The red lines shows the calculated Q_{kinz} values. It was estimated that the $E_{\alpha,\text{max}}$ from the $^{233}\text{U}(\alpha, \alpha')$ reaction deposited approximately 6.3 MeV in the front detector and 20.9 MeV in the back detector, while the $^{233}\text{U}(\alpha, t')$ reaction deposited 2.2 MeV in the front detector and 10.2 MeV in the back detector. These estimates are in agreement with the data.

3.3.1 SiRi particle detector calibration

For the particle spectra calibration, two points in the ^{208}Pb spectra were used: the first excited state from the $^{208}\text{Pb}(\alpha, \alpha')^{208}\text{Pb}$ reaction and the first excited state from the $^{208}\text{Pb}(\alpha, t')^{209}\text{Bi}$ reaction (see arrows in Fig. 3.4). These points were calibrated to fit the expected theoretical Q -values. The Qkinz software [34] was utilized, where the user inputs the desired experimental setup and reaction, and the resulting Q -value and reaction kinematics are estimated. In Fig. 3.5 the Qkinz results are plotted together with the experimental banana plots. Each telescope was calibrated individually, meaning the two peaks highlighted in Fig. 3.4 were found in each of the 64 spectra. Their centroids were located by calculating the weighted mean of the 20 bins with the highest number of counts in the vicinity of the peak.

The resulting gain a and shift b from the ^{208}Pb calibration, were applied with the ^{233}U data. In Fig. 3.5, the $(E, \Delta E)$ bananas are plotted together with the calculated Qkinz values. There can be seen a slight deviation between the data and the Qkinz values in the tritium-banana. At higher energies, the Qkinz-banana has a steeper slope on the up-bend than the experimental banana. The neutron separation energy S_n of ^{233}U is at approximately 5.7 MeV and the peak corresponding to the ground state of ^{233}U is located at approximately 21 MeV. Therefore, the E data up to 15 MeV will not be studied and this deviation can be ignored.

3.3.2 NaI gamma-ray detector calibration

As for the SiRi particle spectra calibration, the NaI(Tl) detectors were calibrated using data from the ^{208}Pb run. Here, reference γ -ray energies from the first excited state of ^{208}Pb at approximately 2.6 MeV and the first excited state of ^{209}Bi at approximately 0.89 MeV were used as points in the linear calibration (see Fig. 3.6). These γ -rays come in coincidence with the detected particles highlighted with arrows in the ^{208}Pb banana-plot in Fig. 3.4. Each peak centroid was found and used as channel numbers in the linear calibration from Eq. (3.2). The peaks, especially in the right panel of Fig. 3.6, are not the obvious choices, and a method of trial and error was used to find the two peaks that gave the best fit with other known γ -peaks. The ^{208}Pb data after the linear calibration is plotted in Fig. 3.7.

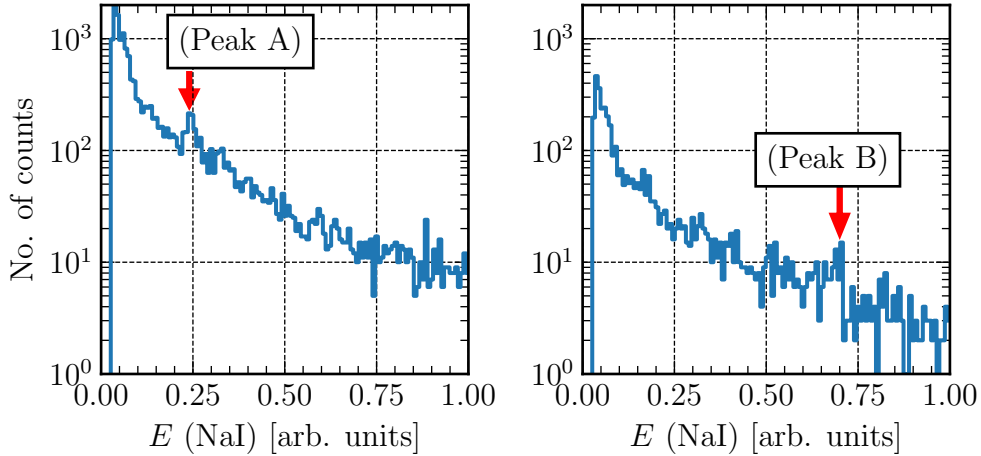


Figure 3.6: *Projections of all the γ -ray detectors.* Left panel: the experimental data sorted with a gate on the $^{208}\text{Pb}(\alpha, t'\gamma)^{209}\text{Bi}$ reaction. (Peak A) points at the 0.89 MeV peak. Right panel: the experimental data sorted with a gate on the $^{208}\text{Pb}(\alpha, \alpha'\gamma)^{208}\text{Pb}$ reaction (Peak B) points at the 2.6 MeV peak (see text).

The resulting gain and shift parameters was applied on the ^{233}U data presented in Fig. 3.8. In this plot, a γ -energy level can be seen at 4-4.5 MeV assumed to belong to the 4.4 MeV excited state of ^{12}C contamination. In the lower panel of Fig. 3.8 a deviation is observed through the 4.4 MeV peaks, which is believed to be linked to the Doppler shift of ^{12}C from the recoil of the 30 MeV α -beam bombardment. Since the ^{12}C peak was not used as a reference, this apparent Doppler shift did not affect the calibration. In fact, assuming it is a Doppler shift, this peak can be used as a confirmation of the calibration.

3.3.3 Time calibration

The final stop of the experimental and calibration work is the (E_γ, E_x) coincidence matrix. Here, detected α -particles are paired with detected γ -rays in true coincidences. To detect these true coincidences, a start signal in the electronic setup is initiated when an α -particle is detected. In this experiment, data was registered for 400 ns after each start signal. Since the beam pulse is shorter than 400 ns, the resulting time-spectrum will contain background measurements of γ -rays from reactions in previous beam-pulses. In Fig. 3.9, the resulting time spectrum is plotted. Two red dashed lines enclose the true coincidence peak, while two red dotted lines enclose a background peak. There is an oscillating tendency in the data, which is directly related to the frequency of the beam pulse. In the analysis, only the data from within the red dashed lines are included and the data within the red dotted lines are subtracted as background measurements.

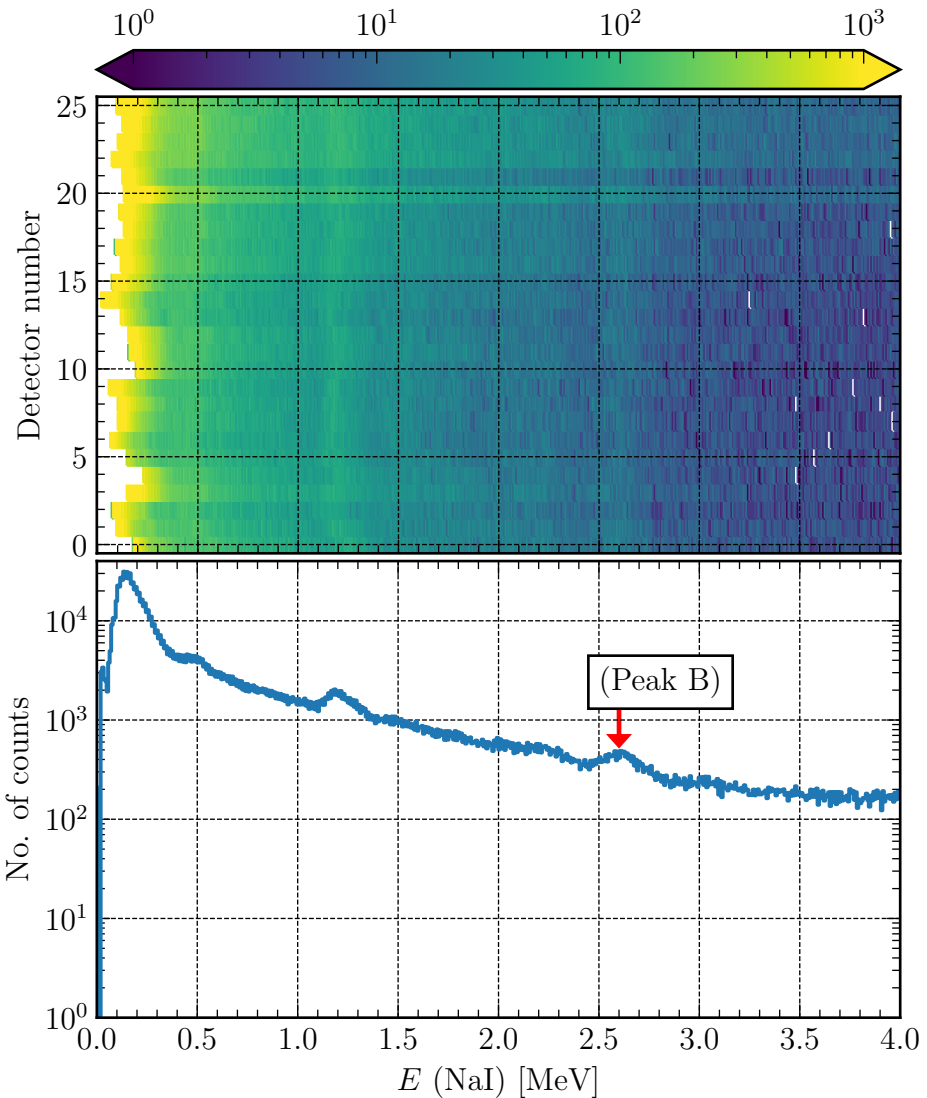


Figure 3.7: *Upper panel:* plots of the γ -ray spectra for all detectors from the ^{208}Pb run after the calibration. *Lower panel:* Projection of upper panel down on the $E(\text{NaI})$ axis. The red arrow shows where (Peak B) from Fig. 3.6 ended up after the linear calibration. The γ -ray annihilation peak at 0.511 MeV is also visible. (Peak A) from Fig. 3.6 is not visible in this ungated plot, but was observed with gate requirements.

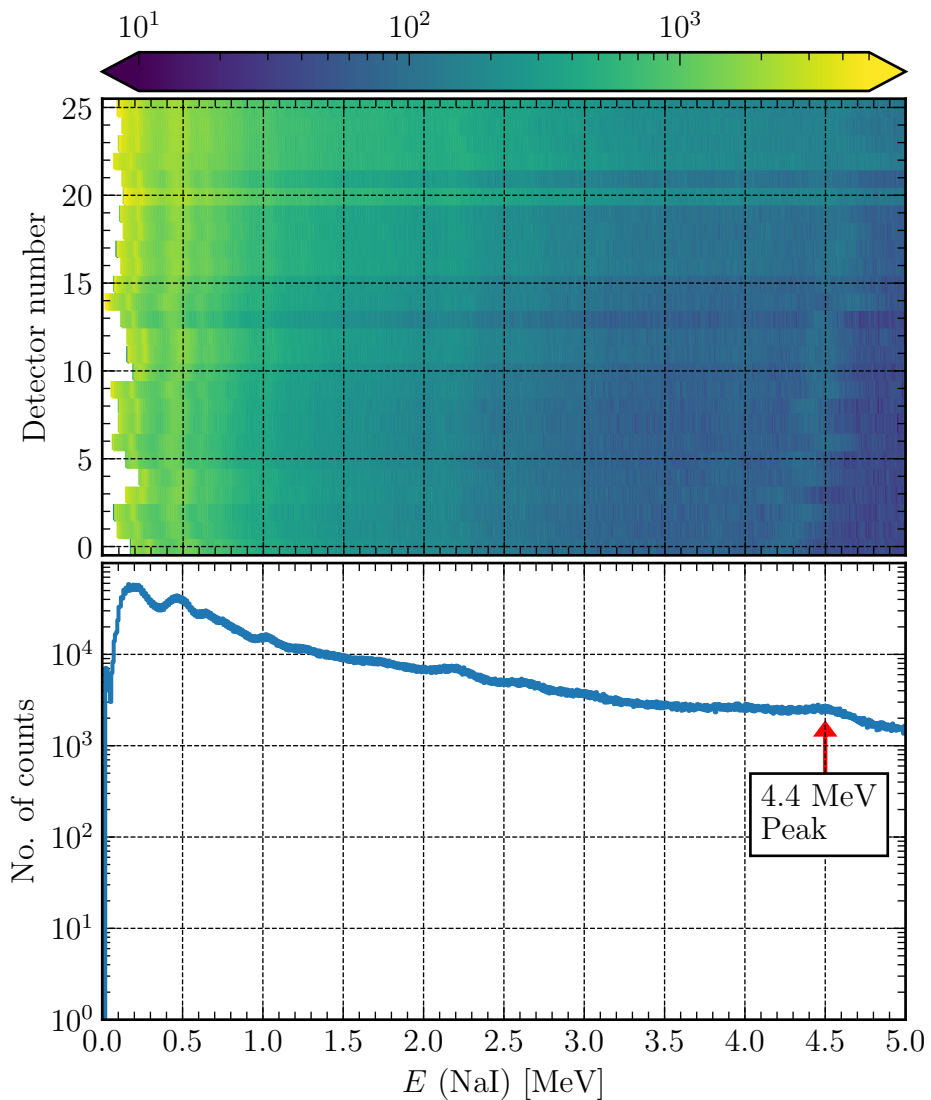


Figure 3.8: *Upper panel:* plots of the γ -ray spectra for all detectors from the ^{233}U run. The 4.4 MeV peak from the ^{12}C contamination and its apparent Doppler shift is visible. *Lower panel:* The $E(\text{NaI})$ counts are projected to the horizontal axis, where the 4.4 MeV and 0.511 MeV peaks are visible.

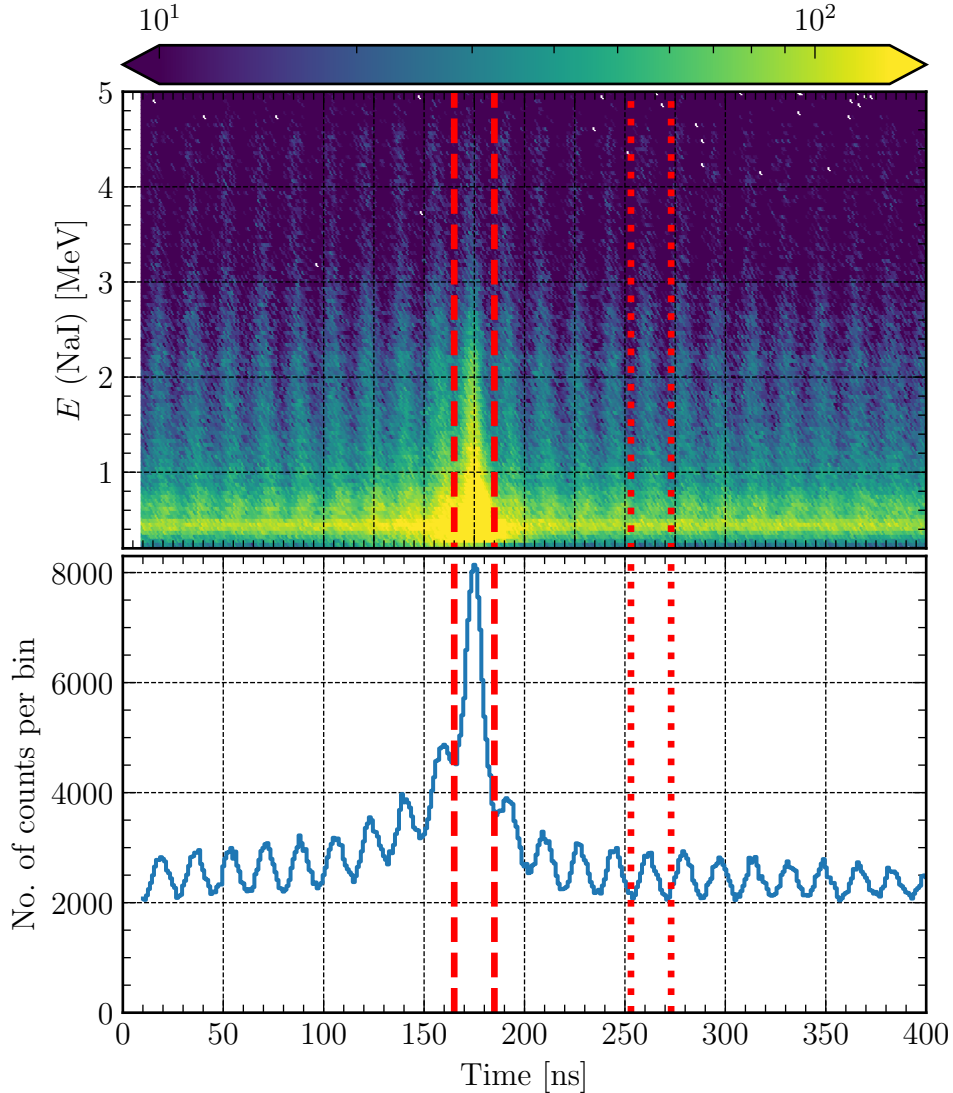


Figure 3.9: *The time vs. energy spectrum in the upper panel and the projection on the time axis in the lower panel. Red dashed lines enclose the true coincidence peak, while red dotted lines enclose the peak used for background subtraction.*

3.3.4 Additional adjustments

After the aforementioned calibration, the E_γ energy was correlated to the E_x excitation energy by applying reaction kinematics, and the (E_γ, E_x) coincidence matrix was extracted from the data. This matrix has the detected excitation-energy E_x of ^{233}U on the vertical axis plotted against the detected

γ -ray energy E_γ on the horizontal axis, as shown in Fig. 3.10. Since the coincidence-matrix is made up of particle- γ coincidences, the resulting γ -rays should not exceed the detected excitation energy of ^{233}U . In other words, a γ -ray sent out from an excited nucleus can not have a higher energy than what the nucleus is excited to. This means that the coincidence-matrix should have a clear diagonal with no data for $E_\gamma > E_x$, except for a few counts as a consequence of experimental limitations.

In Fig. 3.10, one can see that the diagonal plotted with a red dotted line fits the data better than the diagonal from the first calibration attempt, marked with a red dashed line. Also, in the lower panel of Fig. 3.10, the theoretical fission barrier does not match the observed fission barrier. A final adjustment was done by gaining and shifting the E_x axis down so that the diagonal matched the experimental data.

In Fig. 3.11 one can see the new calibrated E_x - E_γ coincidence matrix with an improved $E_\gamma = E_x$ diagonal. The fission-barrier in the lower panel of Fig. 3.11 is also in better agreement with the observed data. Fission reactions can be spotted after the inner fission barrier at 4.35 MeV and increases rapidly around the outer fission barrier at 5.55 MeV, in good agreement with Fig. 4 from Ref. [29]. The final raw coincidence matrix had a total of approximately 80.000 counts.

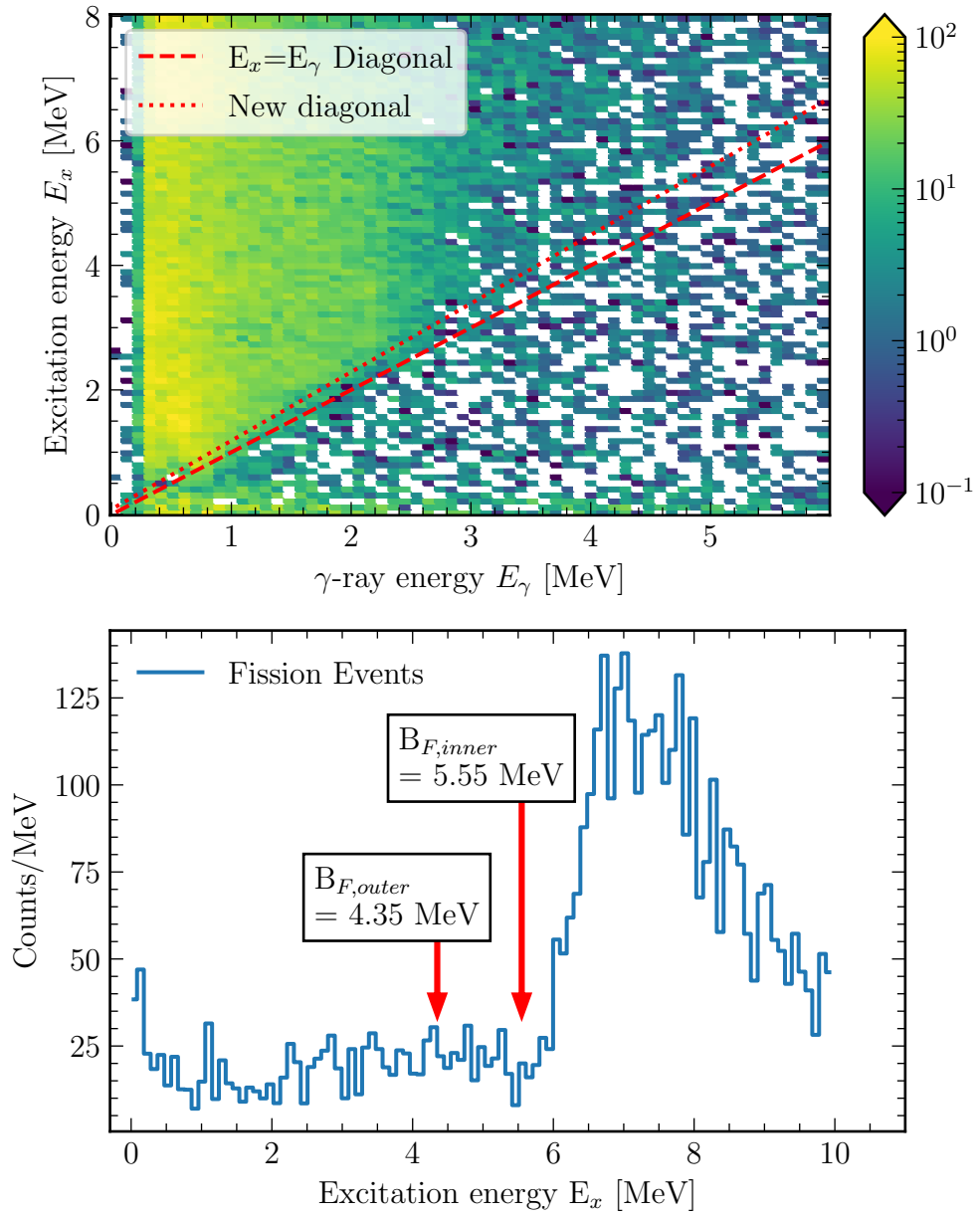


Figure 3.10: *Upper panel:* The raw (E_γ, E_x) coincidence-matrix. The lower dashed line is the $E_x = E_\gamma$ diagonal from the first calibration attempt, while the upper dotted line is what seems to be the true diagonal (see text). *Lower panel:* The (E_γ, E_x) coincidence matrix gated on fission reactions and projected on to the excitation energy axis. The theoretical inner $B_{F,i}$ and outer $B_{F,o}$ fission barrier from RIPL-3 [11] are marked with red arrows.

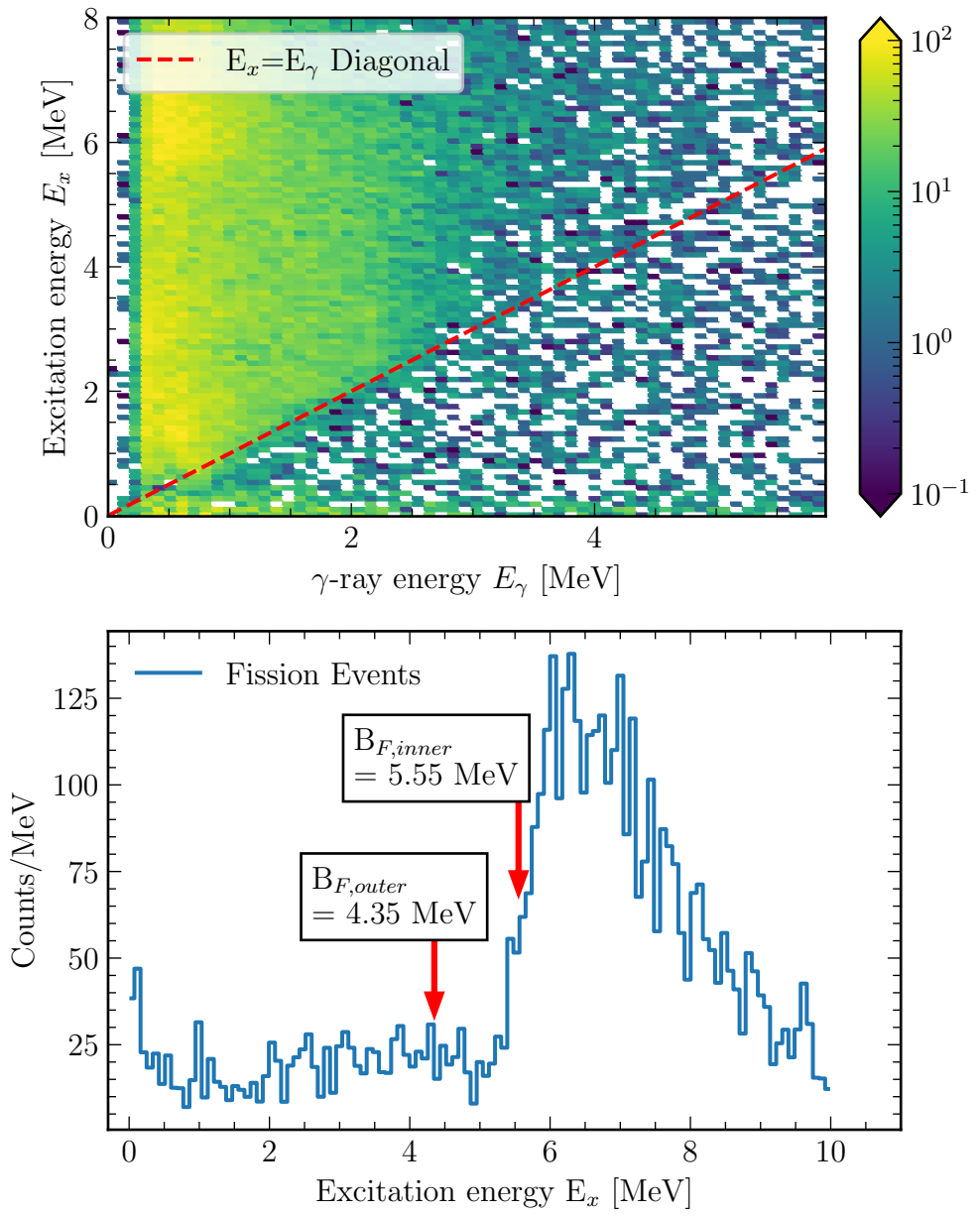


Figure 3.11: *Upper panel:* The raw (E_γ, E_x) coincidence matrix after the diagonal calibration. The true $E_x = E_\gamma$ diagonal is plotted with a red dashed line. *Lower panel:* The (E_γ, E_x) coincidence matrix gated on fission reactions and projected on to the excitation energy axis. The inner and outer fission barriers, marked with red arrows, correlates with previous findings (see text).

Chapter 4

Data Analysis

4.1 Oslo Method

The Oslo method analysis consists of four main steps (1-4) and starts out with the (E_γ, E_x) coincidence matrix. First, the matrix is unfolded to correct for events that do not reveal the full-energy events (1). Following this, the first generation method is applied, where the higher-order generation γ -rays are removed (2). Subsequently, the NLD and γ SF are simultaneously extracted from the first generation matrix (3) and normalized to D_0 and Γ_γ from previous n-capture experiments (4).

4.1.1 Unfolding the (E_γ, E_x) coincidence matrix

When an incoming γ -ray reaches the detector material it reacts in three main ways; photoelectric effect, Compton scattering and pair production. Ideally, the γ -ray is absorbed through the photoelectric effect, transmitting the full energy peak in the measured spectrum. Since this is not the case, the detected γ -ray spectrum contains measurements that are unwanted in the analysis.

Compton scattering happens when an incoming γ -ray is scattered inelastically off the detector material. As a result, a fraction of its energy is transferred to an electron in the material. The transferred energy is decided from the scattering angle of the γ -ray.

If the γ -ray exceeds twice the electron mass-energy with $E_\gamma > 2 \times 511$ keV, pair production might happen. A γ -ray traveling close to a nucleus in the detector material will then spontaneously create an electron-positron pair, and also transfer a small amount of recoil energy to the nearby nucleus. This can result in multiple peaks in the observed spectrum. The positron will quickly annihilate with a nearby electron, creating two new γ -rays, each with an energy of 511 keV. One or both of these γ -rays might escape the detector material, resulting in either the single- or double escape peak at $E_\gamma - 511$ keV and $E_\gamma - 2 \times 511$ keV in the spectrum. If they both are detected, this process contributes to the full energy peak. In addition, a peak at 511 keV will be

observed as a result of background annihilation photons from pair production in surrounding materials.

Desirably, the above-mentioned effects are corrected for in the spectrum used in the analysis. This is done through the unfolding process. The unfolding process used in this analysis was developed by Guttormsen et al. [35] and consist of two main procedures; the *folding iteration method* which removes the unwanted peaks, and the *Compton subtraction method* which removes the Compton background events. Both are briefly described in this section.

A response matrix $\mathbf{R}(E_\gamma, E)$ of the detector setup is used, which represents the probability of a count with the energy E from an incoming γ -ray with the true energy E_γ (see Fig. 4.1). A relation between the observed/folded spectrum f and the unfolded spectrum u is then given by

$$f = \mathbf{R}u. \quad (4.1)$$

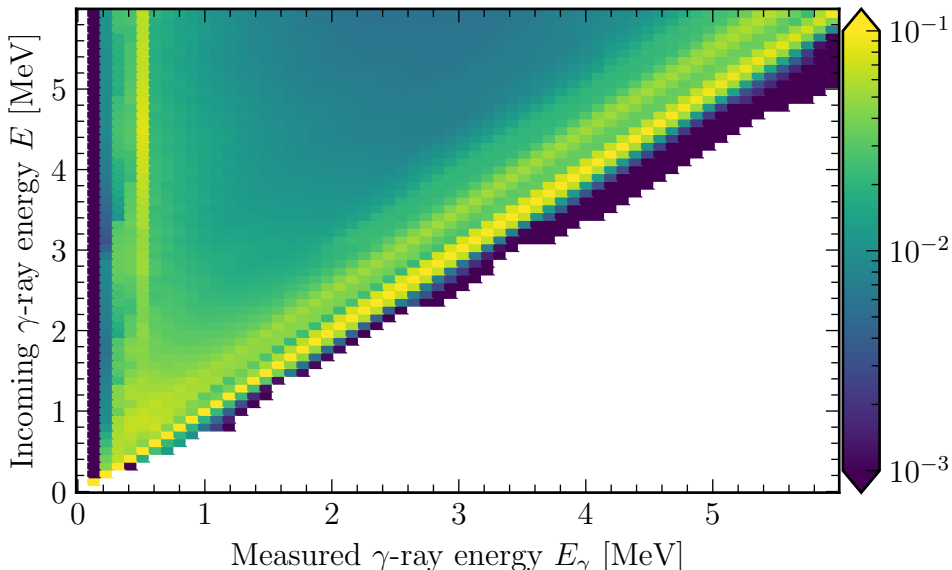


Figure 4.1: The response matrix of the CACTUS detector setup obtained in Ref. [36, 37]. The incoming γ -ray energy is plotted on the y-axis and the measured γ -ray energy is plotted on the x-axis.

One could think that inverting the response matrix to \mathbf{R}^{-1} would easily give the unfolded spectrum u , but this has been shown to cause unwanted oscillations in the unfolded spectrum [35]. Instead, the folding-iteration method is used, where the observed (E_γ, E_x) coincidence matrix is folded with the response matrix multiple times until it is within a satisfactory limit. The steps are as follows:

1. A trial function u^0 is created, where the initial spectrum is used, given by

$$r = u^0. \quad (4.2)$$

2. Then the folded spectrum is created by

$$f^0 = \mathbf{R}u^0. \quad (4.3)$$

3. Subsequently, a new trial function is created by adding the difference between the first-folded and the trial function

$$u^1 = u^0 + (f^0 - r). \quad (4.4)$$

The steps

$$u^{i+1} = u^i + (f^i - r) \quad (4.5)$$

are repeated until f^i can reproduce the observed spectra r , within the desired uncertainties. Approximately 500 iterations was used for this analysis.

After the folding iteration method, the Compton subtraction method was applied to the spectra, thoroughly described in Ref. [35]. Here, the above-mentioned “background” measurements from Compton scattering is removed from the spectra. The idea behind the Compton subtraction method is to use the unfolded spectra to represent the full energy, single escape, double escape, and annihilation peaks and subtract this from the raw spectra to represent the Compton scattering background. The new unfolded spectra is then the raw matrix subtracting the peaks and Compton background. As this method has been discussed in most previous articles and Ph.D./M.Sc. thesis involving the Oslo method (Refs. [9, 15, 35, 38] to name a few), further details will be left out.

4.1.2 Obtaining the First Generation Matrix γ -ray spectra

To extract the NLD and γ SF, one needs the *first generation* γ -rays (sometimes also referred to as *primary γ -rays*). When an excited nucleus de-excites down to its ground state energy, it most likely does so by transferring through different lower energy levels in what is called a cascade. For each de-excitation, the nuclei will send out a γ -ray. The first generation γ -rays represent the first γ -rays that are emitted in this cascade. Because of limits on the experimental timing technique, the unfolded spectra contain all the full-energy peaks from all the cascades. The first generation method from Ref. [39] is applied to the unfolded matrix to obtain the first generation matrix (often denoted as \mathbf{P} , for primary) consisting of only first-generation γ -rays. The general idea behind this method is that if a detected γ -ray is not a first-generation γ -ray, it should also be included in γ -spectra from lower-lying excitation energy bins. With this information, one can subtract

the γ -spectra of lower excitation energy bins from the γ -spectra of higher excitation energy bins in an iterative procedure. One also needs to assume that the γ -decay from any excited state is independent of how the nucleus was excited to this state. This assumption implies that the decay-route of a γ -ray is equivalent, either if it is from a direct reaction or a cascade of higher-lying states.

To explain the first generation method, the notation and description from Refs. [9, 15] is used. The unfolded spectrum is denoted as $AG(E_\gamma)_{E_x}$ and represents the *all-generations* γ -ray spectrum for a given excitation energy E_x . $AG(E_\gamma)_{E_x}$ can be viewed as a superposition of the first generation spectrum $FG(E_\gamma)_{E_x}$ and a weighted sum of the all generation spectra for the lower lying excitation energies, which gives the relation

$$AG(E_\gamma)_{E_x} = FG(E_\gamma)_{E_x} + \sum_{E'_x < E_x} w(E'_x)_{E_x} n(E'_x)_{E_x} AG(E_\gamma)_{E'_x}. \quad (4.6)$$

Turning Eq. (4.6) around, the first generation matrix can be found by

$$FG(E_\gamma)_{E_x} = AG(E_\gamma)_{E_x} - \sum_{E'_x < E_x} w(E'_x)_{E_x} n(E'_x)_{E_x} AG(E_\gamma)_{E'_x}, \quad (4.7)$$

where $n(E'_x)_{E_x}$ is the normalization factor used to correct for the different population cross sections of the excitation energy bins and the weight function $w(E'_x)_{E_x}$ represents the decay probability from E_x to E'_x .

The normalization factor $n(E'_x)_{E_x}$ can be found from the γ -ray spectra using the relation

$$n(E'_x)_{E_x} = \frac{M(E'_x)N(E_x)}{M(E_x)N(E'_x)}. \quad (4.8)$$

Here, M represents the average γ -ray multiplicity and N is the total number of counts. M is estimated from the γ -ray spectra by

$$M(E_x) = \frac{E_x}{\langle E_\gamma \rangle}, \quad (4.9)$$

where $\langle E_\gamma \rangle$ is the weighted average γ -ray energy at E_x .

The weight function $w(E'_x)_{E_x}$ can be understood as the normalized first generation spectra for a given E_x and can be written as

$$w(E'_x)_{E_x} = \frac{FG(E_x - E'_x)_{E_x}}{\sum_{E'_\gamma} FG(E'_\gamma)_{E_x}} \quad (4.10)$$

Using Eq. 4.10, Eq. (4.7) can now be rewritten as

$$FG(E_\gamma)_{E_x} = AG(E_\gamma)_{E_x} - \sum_{E'_x < E_x} \frac{FG(E_x - E'_x)}{\sum_{E'_\gamma} FG(E'_\gamma)_{E_x}} n(E'_x)_{E_x} AG(E_\gamma)_{E'_x}. \quad (4.11)$$

Eq. (4.11) is solved by starting with a set of trial functions for $FG(E_\gamma)$ and iterating until it converges. In Fig. 4.2, the raw, unfolded and first generation

matrices for this analysis are shown. The resulting first-generation matrix was rebinned to approximately 120 keV/bin and 185 keV/bin dispersions for further analysis.

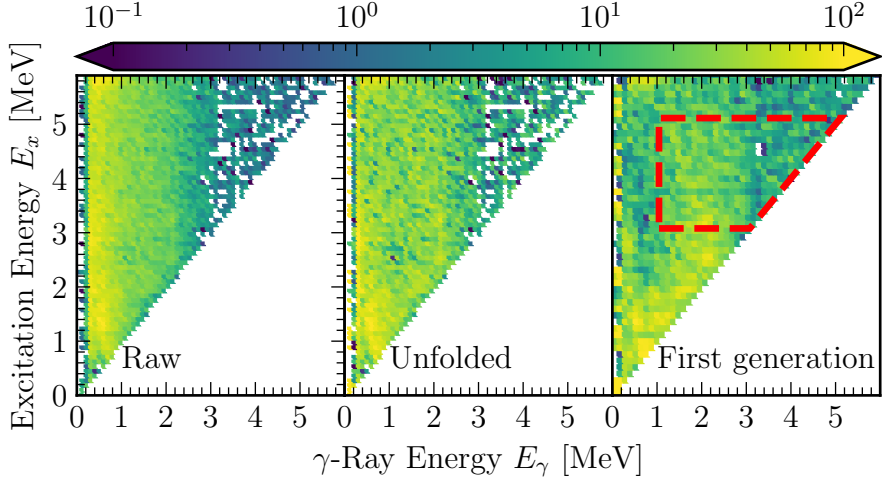


Figure 4.2: From left: the raw, unfolded and first generation matrices. The first generation matrix has been rebinned to 120 keV per bin and the red, stippled trapezoid marks the area where the NLD and γ SF are extracted from, with $E_{x,\min} = 3.1$ MeV, $E_{x,\max} = 5.1$ MeV and $E_{\gamma,\min} = 1.0$ MeV.

4.1.3 Extracting the NLD and γ SF

Extracting the NLD and γ SF from the first-generation matrix is done with the relation

$$\mathbf{P}(E_x, E_\gamma) \propto \rho(E_f = E_x - E_\gamma) \mathcal{T}(E_\gamma) \quad (4.12)$$

where $\mathbf{P}(E_x, E_\gamma)$ is the first generation matrix, $\rho(E_f = E_x - E_\gamma)$ is the level density and $\mathcal{T}(E_\gamma)$ is the transmission coefficient (related to the strength function by Eq. (2.13)). Eq. (4.12) stems from Fermi's golden rule given by Eq. (2.15) and a heavy relation on the gBA hypothesis, as discussed in Sec. 2.2. With this in place, one can relate the first generation matrix $\mathbf{P}(E_x, E_\gamma)$ to λ and the transmission coefficient \mathcal{T} to $|\langle f | \hat{H} | i \rangle|^2$, and extract ρ and \mathcal{T} from the first generation matrix. The extraction is done by a χ^2 -minimization of the equation

$$\chi^2 = \sum_{E_x, E_\gamma} \left(\frac{\mathbf{P}_{\text{exp}}(E_x, E_\gamma) - \mathbf{P}_{\text{fit}}(E_x, E_\gamma)}{\sigma_{\mathbf{P}_{\text{exp}}}(E_x, E_\gamma)} \right)^2 \quad (4.13)$$

from Ref. [6], with notation from Ref. [15] where $\sigma_{\mathbf{P}_{\text{exp}}}(E_x, E_\gamma)$ is the standard deviations of the experimental spectra.

In Fig. 4.2, the red dashed trapezoid shows the area the ρ and \mathcal{T} are extracted from. The limits on E_x and E_γ were decided so that

- the lower limit of the E_x fulfills the requirement of compound decay,
- the upper limit of the E_x is low enough so that γ -decay is the only channel,
- the lower limit of E_γ excludes “leftovers” from higher generation γ -rays [6].

Fig. 4.3 shows the extracted $\rho\mathcal{T}$ plotted together with experimental points from the first generation matrix for a selection of excitation energies E_x . This figure confirms the successful extraction as the $\rho\mathcal{T}$ product and the first generation data are in good agreement.

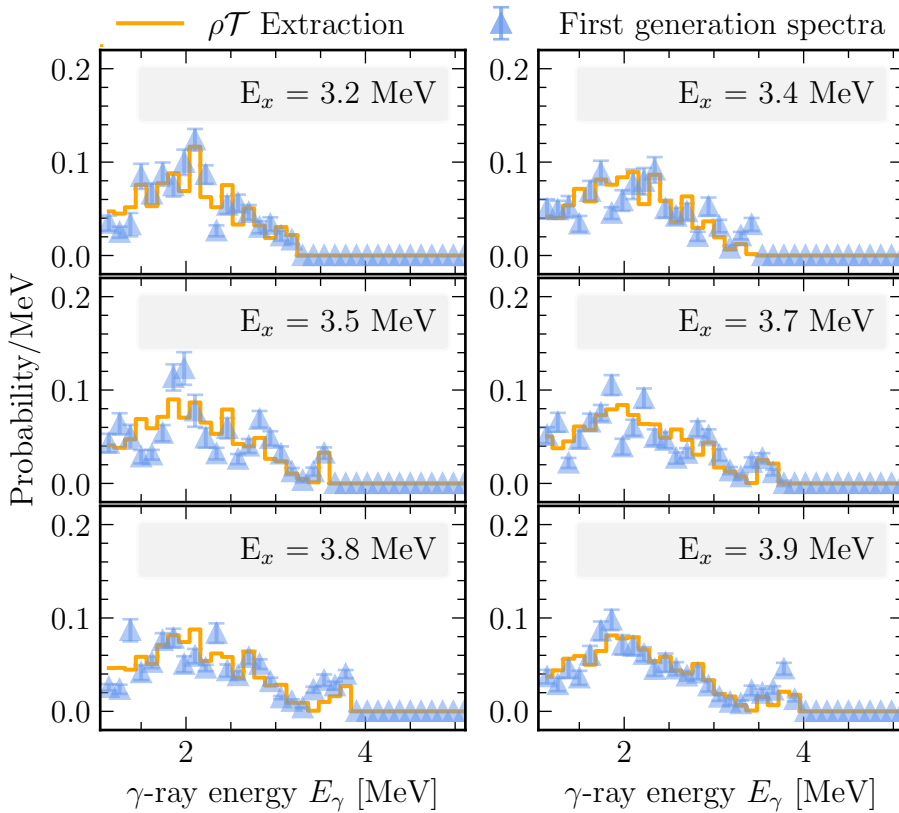


Figure 4.3: Blue triangles shows data from the first generation matrix. The orange line is the product of the extracted ρ and \mathcal{T} . Each plot is gated on a certain excitation energy bin, and shows the number of counts and correlating E_γ for the given excitation energy.

Any other $\tilde{\rho}$ and $\tilde{\mathcal{T}}$ given by [8]

$$\tilde{\rho}(E_x - E_\gamma) = A \exp [\alpha(E_x - E_\gamma)] \rho(E_x - E_\gamma) \quad (4.14)$$

$$\tilde{\mathcal{T}}(E_\gamma) = B \exp[\alpha E_\gamma] \mathcal{T}(E_\gamma), \quad (4.15)$$

with A , B and α being parameters, give the same fit to the first-generation matrix. Thus, these parameters yields an infinite number of solutions to the first generation matrix. Hence, the extracted values need to be normalized to previous data, which is the topic of the following section.

4.1.4 Normalizing the NLD and γ SF

The starting point for the normalization is Eqs. (4.14) and (4.15). For Eq. (4.14), the extracted data is fit to known, discrete energy levels at lower excitation energy. At higher energies, the level density is calculated at the neutron separation energy S_n . Usually, the extracted data does not reach up to S_n , and an extrapolation between a selection of points in ρ up to $\rho(S_n)$ is done. In this work, the CT model from Eq. (2.6) was used for the extrapolation. The derivation of $\rho(S_n)$ from Ref. [8] yields the equation

$$\rho(S_n) = \frac{2\sigma^2}{D_0} \frac{1}{(I_t + 1) \exp[-(I_t + 1)^2/2\sigma^2] + I_t \exp[-I_t^2/2\sigma^2]}, \quad (4.16)$$

where I_t is the target nucleus spin, σ is the spin-cutoff parameter and D_0 is the average neutron resonance spacing. σ was introduced in Sec. 2.1, and found using the EB05 model. D_0 and I_t is taken from Ref. [11] and the level density parameter a , used to calculate σ , is taken from Ref. [40].

For Eq. (4.15), the previously measured average radiative width $\langle \Gamma_\gamma \rangle$ at the neutron separation energy S_n is used to find the slope of \mathcal{T} related to the normalization parameter B by

$$\langle \Gamma_\gamma(S_n) \rangle = \frac{D_0}{2\pi} \int_0^{S_n} dE_\gamma B \mathcal{T}(E_\gamma) \times \rho(S_n - E_\gamma, J) \sum_J g(S_n - E_\gamma, J), \quad (4.17)$$

from Ref. [12]. The $\langle \Gamma_\gamma \rangle$ parameter does not exist as previous data for ^{233}U . When this has been the case in previous Oslo method analysis, one calculated the mean $\langle \Gamma_\gamma \rangle$ from the nearby isotopes as discussed in Ref. [9]. The same approach was made in this work.

4.2 Implementation - OMpy

A collection of programs for the Oslo method analysis is put together and denoted the Oslo method Software (OMS) in this work. This method and software were developed by Guttormsen, Schiller et al. [41] and applied to most previous Oslo method analysis.

For this work, the new Python implementation of the Oslo method software was used. The new software is named Oslo method Python (OMpy) and developed by Eriksson, Zeiser, and Lima et al. [9]. Because this software

is rather new, the results were compared to results from the standard OMS. The motivation for the new software is explained in Ref. [15], and stems from both creating a more user-friendly experience and the lack of a proper $\sigma_{\mathbf{P}_{\text{exp}}}(E_x, E_\gamma)$ matrix from Eq. 4.13.

A new, more thorough error propagation is applied in OMpy, using an ensemble-based Monte Carlo technique. An ensemble of randomly perturbed copies of the experimental raw (E_γ, E_x) coincidence matrix is created. It is assumed that each bin i of the experimental raw matrix is independent and follow the Poisson distribution given by

$$\mathcal{P}_\lambda = p(k|\lambda) = \frac{\lambda^k e^{-\lambda}}{k!}. \quad (4.18)$$

Here, $p(k|\lambda)$ is the probability of drawing k with the expected value λ . A copy of the raw matrix was made by randomly drawing a number for each bin i in the new copy. The number was produced by setting the λ parameter equal to the number of counts in the corresponding bin i in the raw matrix. A hundred different ensemble members were created for this analysis, resulting in hundred different realizations of the experiment. With this method, the sample mean and the standard deviation can easily be calculated for in each bin for all ensemble members throughout the unfolding, first-generation, and extraction methods. This leads to a more proper $\sigma_{\mathbf{P}_{\text{exp}}}(E_x, E_\gamma)$ matrix from Eq. 4.13 used when extracting the NLD and γ SF.

With the OMS, the user chooses a spin-cutoff model and previous experimental input parameters. In this work, the EB05 spin-cutoff model was chosen with the shift parameter E_0 and temperature parameter T . With OMpy, the spin-cutoff model parameters are by default included in the normalization procedure, together with A , B and α from Eqs. (4.14) and (4.15), in order to find the NLD extrapolation up to $\rho(S_n)$. Therefore, the presented E_0 and T parameters in Tab. 4.1 are the applied normalization parameters in the OMS analysis and the starting values of the normalization parameter in the OMpy normalization procedure.

Table 4.1: *Parameters used in the Oslo method normalization and extraction. D_0 was taken from Ref. [11]. E_0 was taken from Ref. [40]. $\langle\Gamma_\gamma\rangle$ is the average value of nearby nuclei from Ref. [11]. The range of the temperature parameter T was chosen from previous Oslo method analysis. For the OMS implementation, the temperature parameter was set to $T = 0.39$ MeV.*

Normalization Parameters			
$\langle\Gamma_\gamma\rangle$	D_0	T	E_0
[meV]	[eV]	[MeV]	[MeV]
24.2(53)	4.6(7)	0.2-0.5	-0.519

OMpy utilizes a maximum log-likelihood estimation to find the normalization parameters. This leads to a sum of χ^2 minimizations between the

known normalization parameters and the extracted ρ and \mathcal{T} . For example, the χ^2 minimization of the known discrete levels is given by

$$\chi_{discrete}^2 = \sum_j \left(\frac{\rho_{j,discrete} - \rho_{j,Oslo}(\theta)}{\sigma_j} \right)^2, \quad (4.19)$$

where $\rho_{j,discrete}$ is the level density for the known discrete levels, $\rho_{j,Oslo}(\theta)$ is the level density in the discrete energy region for the extracted data with uncertainty σ_j . Unlike OMS, OMpy uses a simultaneous normalization of the NLD and γ SF, to make sure the same parameters are used for both normalizations, hence the sum of χ^2 minimizations. An approximate solution to the likelihood is found with a differential evolution minimizer (DE). For this work, a boundary was set on the normalization parameter T to stay within 0.2-0.5 MeV for the initial guess, based on values from previous analysis [42]. The DE results are used as weakly informed priors to the Bayesian nested sampling algorithm MultiNest [43]. All the priors were kept as in Sec. 6.3 in Ref. [9], except for prior of the normalization parameter α . It was found that the initial definition of its log-uniform prior facilitated invalid normalization results. This issue is investigated in Appendix A and was avoided by setting a boundary on the α parameter prior between 1 and 2^4 . MultiNest then makes a number of samples for each ensemble member. For this analysis a total of 400 samples were used, by the recommendation in Ref. [44]. Following this, the resulting uncertainty is the combination of the i different samples and the m different ensembles. The resulting OMpy data is the median of all the ensemble results, with a 68% confidence interval.

In the raw matrix, sometimes zero-experimental counts are present and OMS and OMpy treat these cases differently. OMS puts an uncertainty on the zero count bins in the raw (E_γ, E_x) coincidence matrix, based on the counts of the bins in its vicinity. In OMpy, the number of counts in each bin of the ensemble members are drawn from the Poisson distribution from Eq. (4.18). The bins with zero counts will then be zero for all ensemble members, and hence creating the least uncertain bins through the analysis. Similarly, bins with few counts will also be relatively certain, based on the Poisson distribution for a low expected value. Two methods of working around this outcome were investigated in this analysis. One workaround was to create a large enough dispersion in the first generation matrix in an attempt to level out the bins with zero or few counts. The other workaround involved removing the resulting γ SF values that arose due to this aspect in further investigation of the SR, following the ^{164}Dy example in the OMpy article.

⁴Note that the boundary on α is for the MultiNest algorithm, while the previously mentioned boundary on T was for the DE results which work as priors for MultiNest. Although boundaries were set on T , MultiNest facilitated wrong results, and hence the boundary was set on α .

Chapter 5

Results and discussion

In the following sections, the resulting γ SF and NLD with energy dispersion of 120 keV/bin and 185 keV/bin are presented for both the OMpy and OMS analysis. Also, the strength and centroid of the observed scissors resonance is extracted from the γ SF. The SR mode has been investigated in three different ways. An iterative fitting procedure was utilized with both dispersions of 120 keV/bin and 185 keV/bin. Since these two methods produced similar plots and fit parameters, the figures from the 185 keV/bin dispersion fit is included in Appendix B and only the SR results are presented in the following. In addition, a less constrained fitting procedure was utilized with the 120 keV/bin data as well.

5.1 γ SF and NLD

As mentioned in Ref. [9], different dispersion and fit-ranges can be applied for the Oslo method normalization procedure. In this work, different dispersions were investigated when performing the Oslo method analysis in order to level out bins with few or no counts. The fit regions mark the areas where the NLD and γ SF are extrapolated from in the normalizing procedure. Different fit-regions were used for OMpy and OMS, in order to get the best correlation between the results from the two software implementations. A method of trial and error was used, where the OMpy results were first normalized with a chosen fit region. Following this, different OMS fit regions were tested to find a good correlation with the OMpy results. Deviations between the OMpy and OMS results are discussed in the following.

In Fig. 5.1, the NLD and γ SF results with a 120 keV/bin dispersion are presented and the two Oslo method implementations are compared.

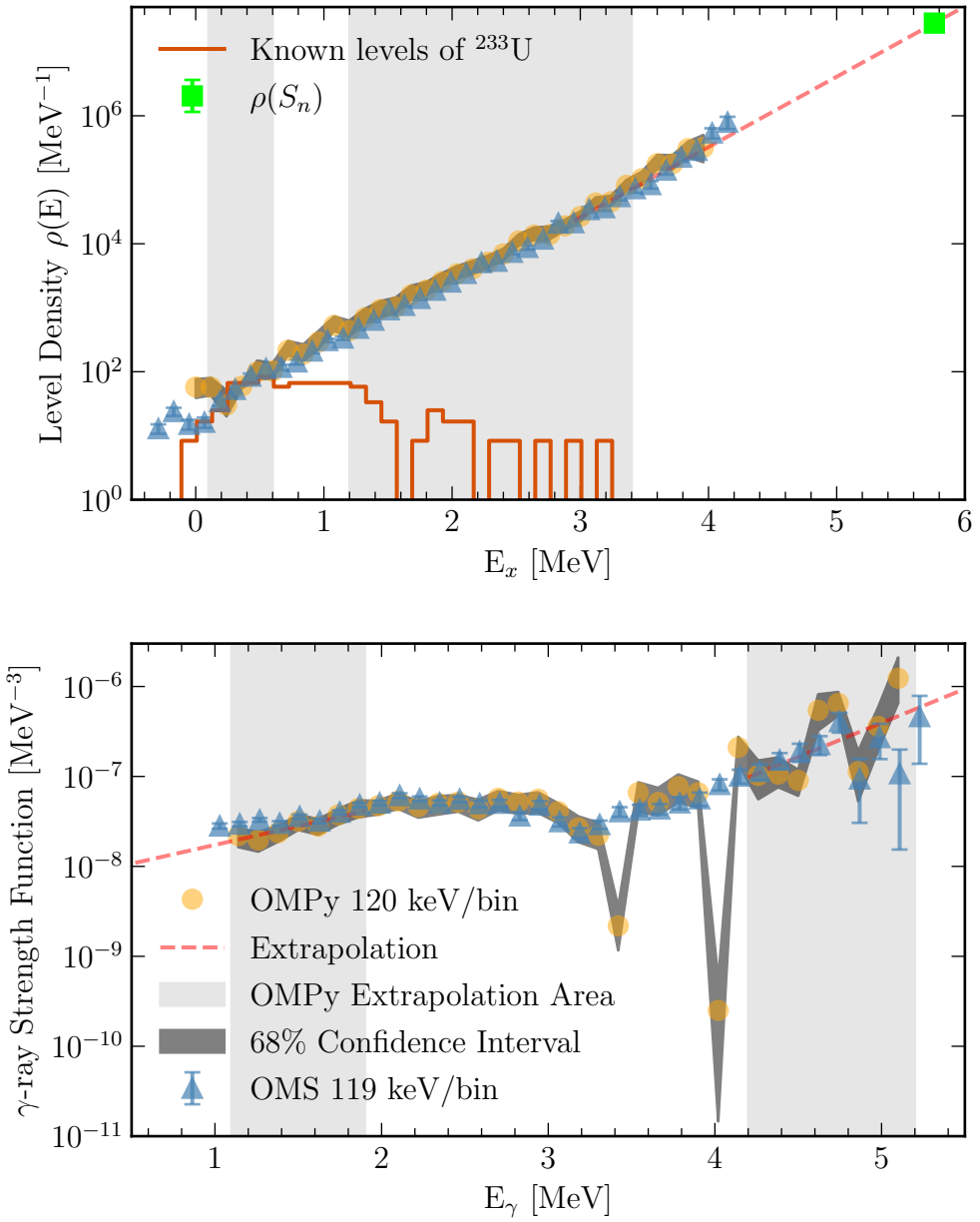


Figure 5.1: The γ SF and NLD from OMS in blue triangles and OMpy in orange circles with dispersion of 120 keV/bin for both E_x and E_γ . The OMpy results are presented with a 68% confidence interval marked with a dark gray band. The upper panel shows the NLD, with the known discrete levels from Ref. [11] as a red, solid line and $\rho(S_n)$ as a green square. The lower panel shows the γ SF. In both panels, the OMpy extrapolation are showed as red, stippled lines and their respective extrapolation areas are marked with light gray.

The two dips in the γ SF data in Fig. 5.1 are obvious at approximately 3.4 and 4 MeV, and reflect the different treatments of bins with few, or zero, counts in the (E_γ, E_x) coincidence matrix for the two methods, as introduced in Sec. 4.2. The areas of the γ SF that are not affected by this, show a good correlation between OMS and OMpy. Because of the dips, the γ SF from OMpy were rather sensitive to the extrapolation areas. Since the dips are the most certain points, they are the most significant in the weighted extrapolation. The high E_γ extrapolation area in the γ SF was chosen to eliminate these dips from the extrapolation.

To level out the bins with few or no counts, the dispersion was increased by increments of approximately 5 keV/bin until reaching a satisfactory result. The 185 keV/bin dispersion results are plotted in Fig 5.2. As with the 120 keV/bin dispersion, the γ SF normalization up to 3 MeV shows a good correlation between the two implementations. However, with the 185 keV/bin dispersion, the OMpy data are approximately up to a factor of 5 larger than the OMS data above 3 MeV. Different extrapolation areas were tested, but this did not affect the deviation. As the Scissors Resonance probably lies around 1.5 – 3 MeV, this deviation could cause a higher GDR tail resulting in a somewhat lower SR strength than the 120 keV/bin dispersion results.

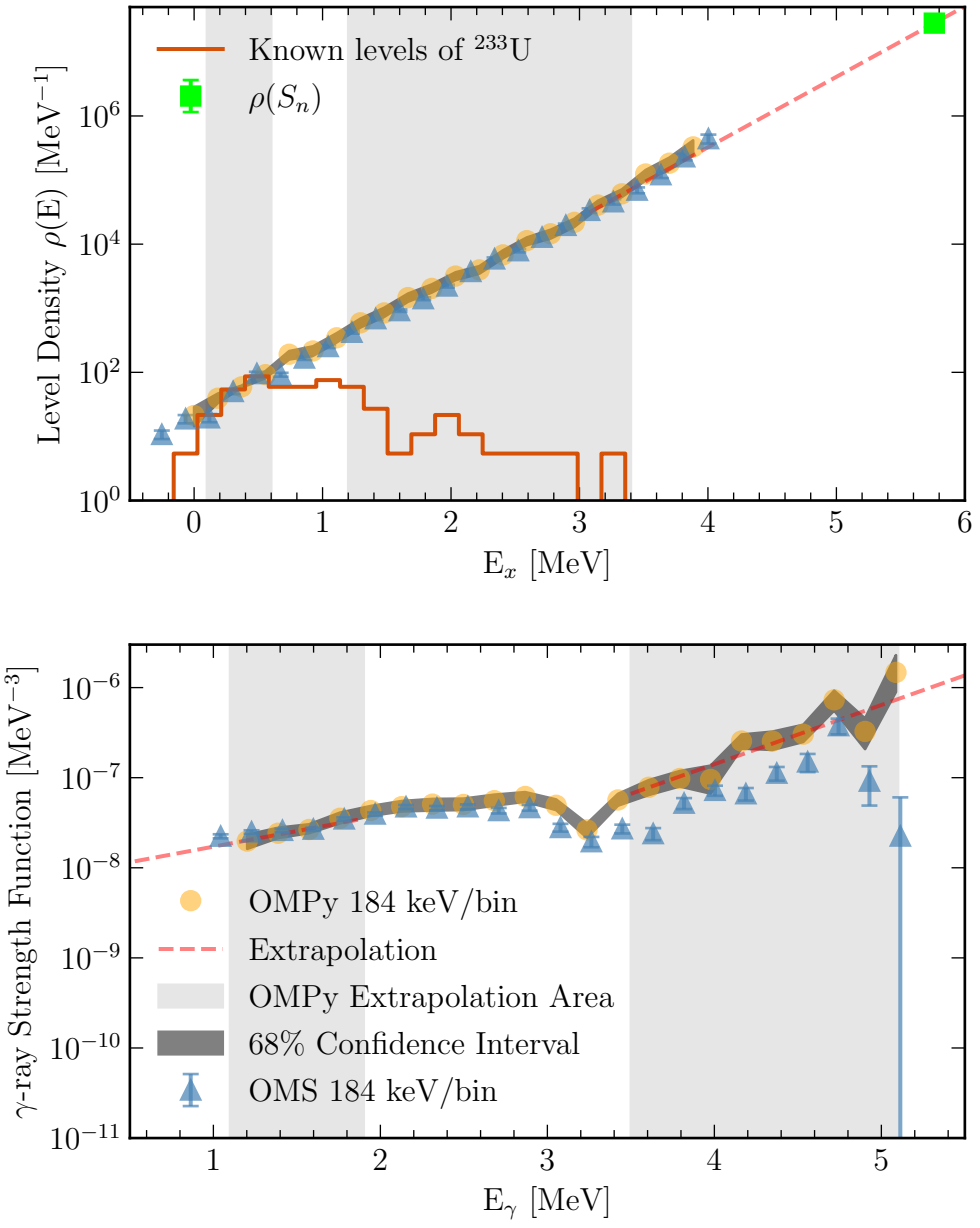


Figure 5.2: The γ SF and NLD from OMS in blue triangles and OMpy in orange circles with dispersion of 185 keV/bin for both E_x and E_γ . The OMpy results are presented with a 68% confidence interval marked with a dark gray band. The upper panel shows the NLD, with the known discrete levels from Ref. [11] as a red, solid line and $\rho(S_n)$ as a green square. The lower panel shows the γ SF. In both panels, the OMpy extrapolation area is shown as red, stippled lines and their respective extrapolation areas are marked with light gray.

5.2 Scissors Resonance

The low energy tail of the higher-lying resonances was subtracted from the γ SF, to measure the $B_{SR}(M1)$ strength of the scissors resonance. Previous data from Berman et al. [45] and RIPL-2 [46] were used together with the γ SF from this work to fit the Giant Dipole Resonance (GDR), the Pygmy Dipole (PDR), and Spinflip (SFR) resonances.

Two different fitting methods are investigated. One method strictly constrained several resonance parameters and fit the different resonances in an iterative procedure. This method was performed with both the 120 keV/bin and 185 keV/bin dispersion results. In addition, a method with less constraints on the resonance parameters was carried out with the 120 keV/bin dispersion results.

The two dipping points from the γ SF with a 120 keV/bin dispersion were removed in the fitting procedure, following the ^{164}Dy example in the OMpy article [9]. The fit was done by using a least-square method to minimize the sum of squared residuals between the GLo or SLo and the experimental γ SF from this and previous work⁵.

In the iterative procedure, the GDR was first fit with two GLo functions given by Eq. (2.17) within a restricted range as seen in Fig 5.3. The GLo temperature parameter was fixed at $T_f = 0.2$ MeV as done in previous actinide analysis utilizing the Oslo method [47]. It was seen that the GDR fit is somewhat sensitive to the T_f parameter, and a larger value resulted in a larger tail, which followingly will yield a lower SR strength.

Following the GDR-fit, an unknown PDR and SFR were fit between the GDR and the SR energy regions. Both were fit using SLo functions from Eq. (2.19). One should notice the lack of, and relatively uncertain, data in the relevant 3-10 MeV energy region. These resonances were included in the fit due to their historical presence in most previous scissor resonance analyses, and hence to create a reasonable GDR tail. The resulting PDR and SFR resonance parameters were strictly constrained and therefore presented without uncertainty in Tab. 5.1. As these parameters are not relevant in this analysis, other than extracting a reasonable GDR tail, they will not be discussed further. In Fig 5.4 one can see the fit-area and resulting PDR and SFR resonances.

⁵With this fitting method, the input γ SF errors had to be symmetrical around the data. Since the OMpy data are presented with a confidence interval, rather than symmetrical error bars, the error was represented by the lower or upper interval with the largest deviation from the median.

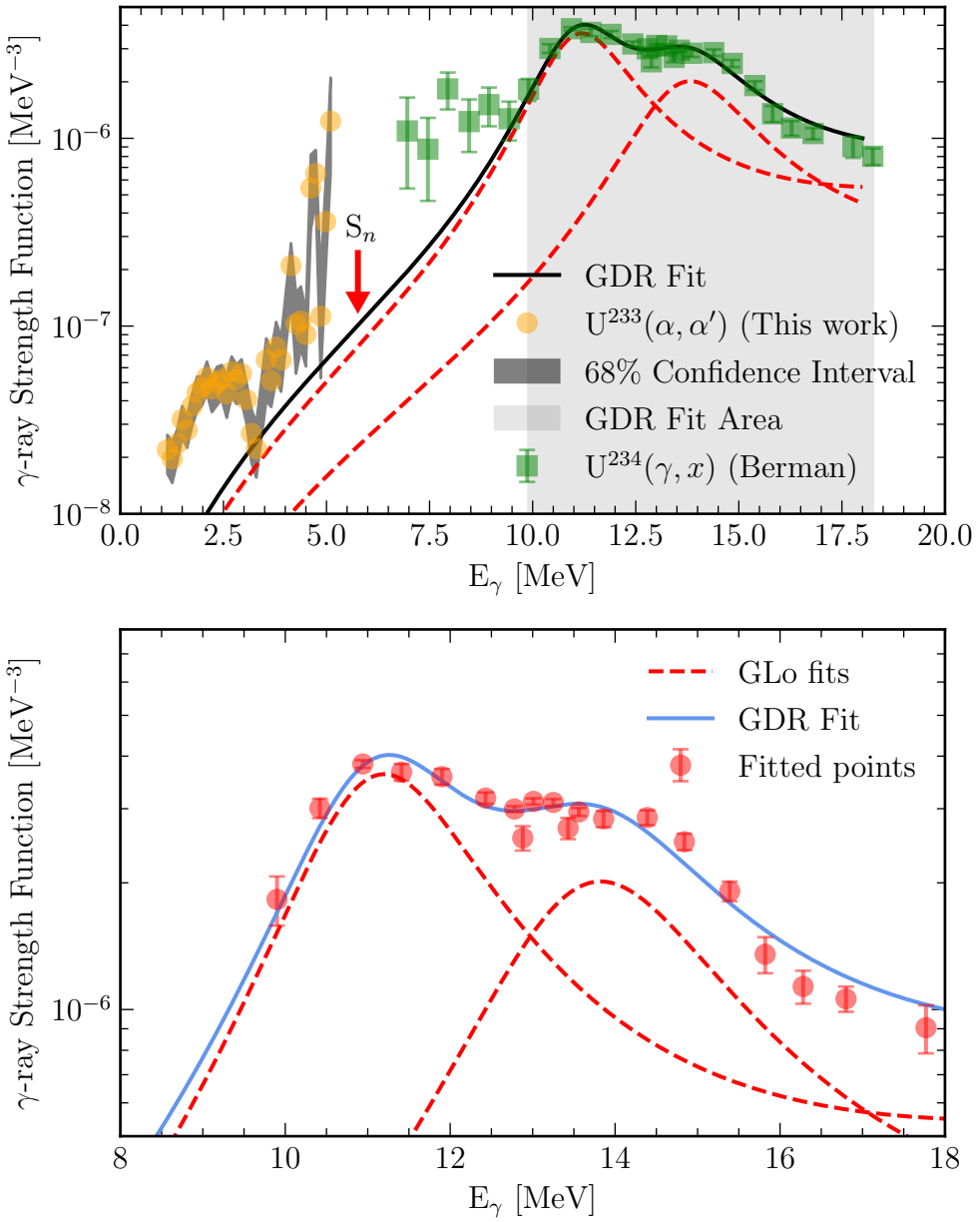


Figure 5.3: *Upper panel:* The red stippled lines show the fit of the two GDR peaks and the black solid line shows the total fit. The orange circles show the γ SF from this work with a dispersion of 120 keV/bin and its uncertainty as the dark gray 68% confidence interval. The green squares are the cross-section data from Ref. [45] converted to γ SF by Eq. (2.14). The light gray area encloses the energy interval in which the GDR peaks were fit. *Lower panel:* Blue solid line shows the total GDR fit. The red points were used in the GDR fit.

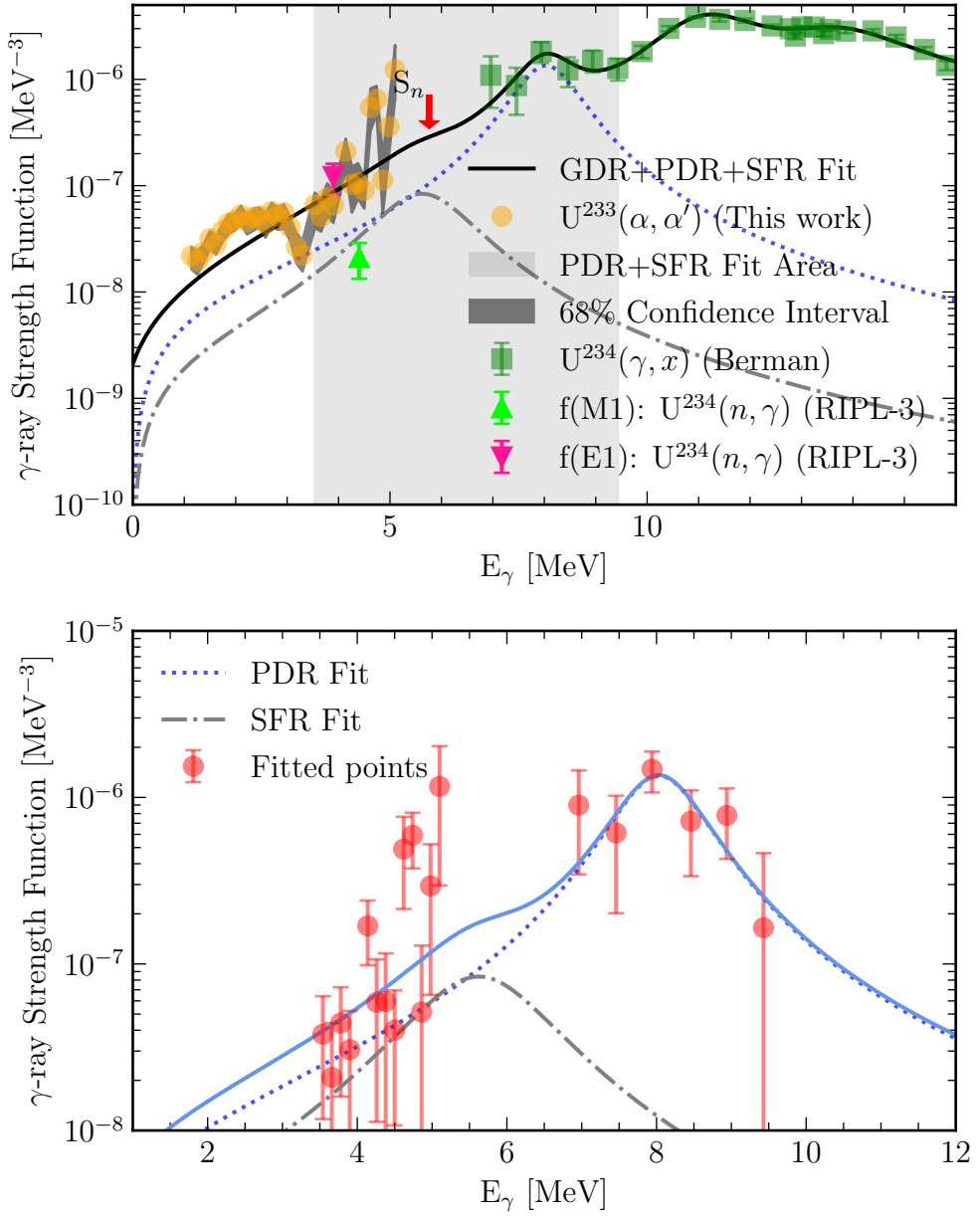


Figure 5.4: *Upper panel:* Solid line shows the total $GDR+PDR+SFR$ fit. A blue dotted line shows the PDR fit and a grey stippled dotted line shows the SFR fit. The orange circles show the γSF from this work with a dispersion of 120 keV/bin and its uncertainty as the dark gray 68% confidence interval. The pink and green triangles taken from RIPL-2 data were not used as points in the fit but correlates well with the fit and the data. *Lower panel:* The blue solid line shows the $PDR+SFR$ fit. The red points are a combination of the γSF from this work and the data from Ref. [45] used to fit the PDR and SFR .

Table 5.1: *Giant Dipole, Pygmy and Spinflip resonance parameters from the more constrained fit with a 120 keV/bin dispersion.* ω , σ and Γ represents the centroid, cross section and FWHM of the given resonance peak. For the GDR, the temperature parameter was fixed at $T_f=0.2$ MeV. See text for more information about the PDR and SFR parameters.

Giant Dipole Resonance					
$\omega_{E1,1}$	$\sigma_{E1,1}$	$\Gamma_{E1,1}$	$\omega_{E1,2}$	$\sigma_{E1,2}$	$\Gamma_{E1,2}$
[MeV]	[mb]	[MeV]	[MeV]	[mb]	[MeV]
11.4(2)	453(24)	2.6(5)	14.08(6)	310(37)	3.2(6)
Pygmy Resonance			Spinflip Resonance		
ω_{PDR}	σ_{PDR}	Γ_{PDR}	ω_{SF}	σ_{SF}	Γ_{SF}
[MeV]	[mb]	[MeV]	[MeV]	[mb]	[MeV]
8.1	111.8	1.5	7.1	11.1	2

The $B_{SR}(M1)$ strength was found by integrating the median experimental γ SF from OMpy by Eq. (2.20), after subtracting the GDR+PDR+SFR tail. The uncertainty of the strength is given by a range which was found by integrating over the lower and upper part of the 68% confidence interval, as shown in Fig 5.5. A similar uncertainty range of the $B_{SR}(M1)$ was presented in Ref. [48].

In addition to the iterative fitting procedure, where the resonance parameters of the PDR and SFR were strictly constrained, a method of fitting the data with less constraints were done with the 120 keV/bin dispersion. The ω_{PDR} and ω_{SFR} centroids were bound between 4-9 MeV and the ω_{SR} centroid were bound between 1.5-3.5 MeV, based on previous analysis [25, 49]. The resulting resonance parameters and their boundaries can be seen in Fig. 5.6 and Tab. 5.2 and were more or less free. Note that as for the iterative method, the PDR and SFR resonance parameters are presented without uncertainties in Tab. 5.2. As a consequence of the uncertain, and lack of, data in the relevant energy interval, these parameters proved to be highly uncertain. In Fig. 5.7 the full GDR fit is presented including the underlying PDR, SFR, and SR. The resulting scissors resonance and its integral area are presented in Fig. 5.8.

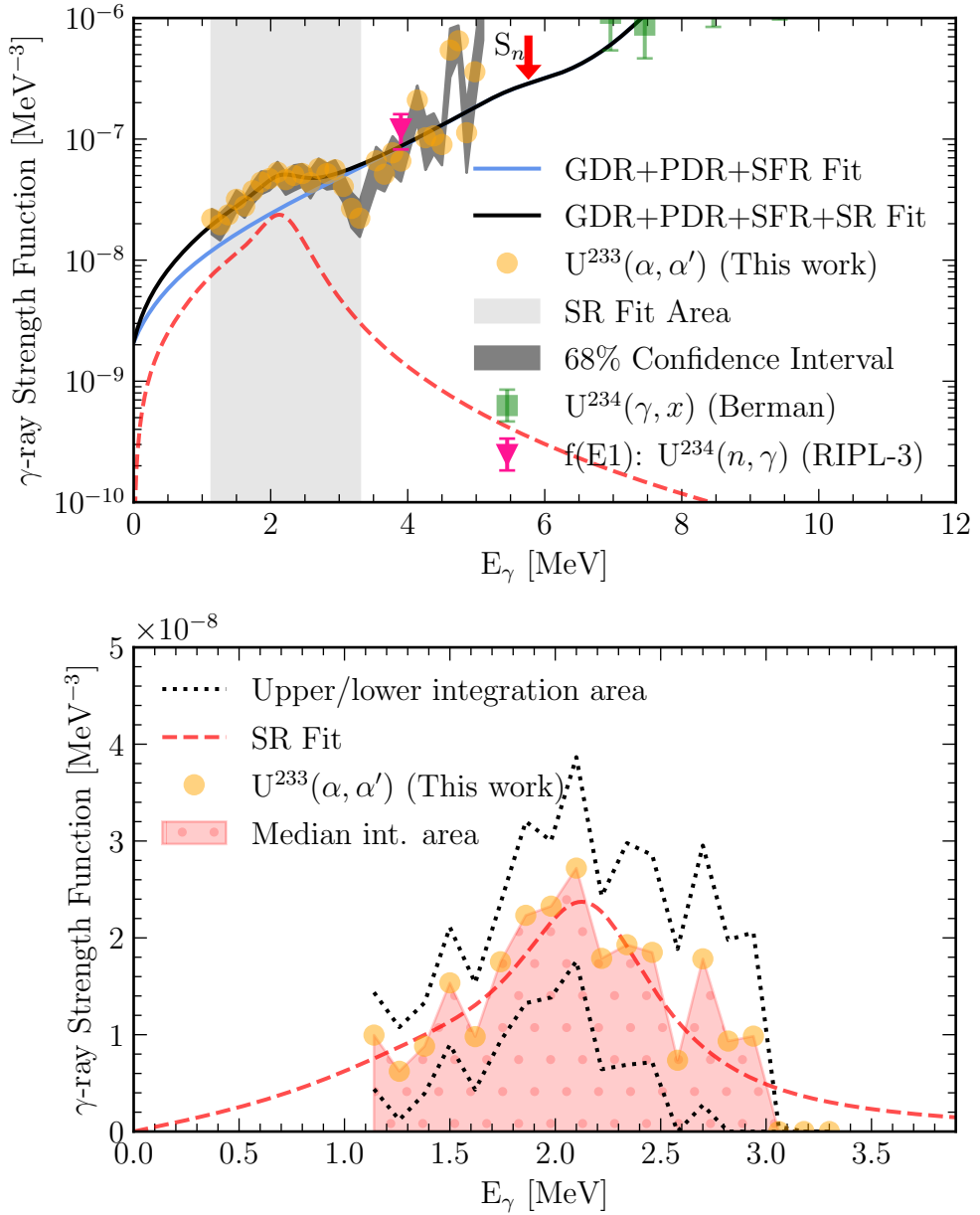


Figure 5.5: Upper panel: Black solid line shows the total $GDR+PDR+SFR+SR$ fit and in the blue solid line the SR fit is excluded. Lower panel: The red area enclose the integration area used to find the strength of the SR. Black dotted lines show the upper and lower integration areas used to find the uncertainty of the SR strength. Orange circles shows the median γ SF from OMpy with a 120 keV/bin dispersion after the $GDR+PDR+SFR$ tail was subtracted. Note that the fit of the SR is plotted as a red dashed line in the upper and lower panel, but it is not used in further analysis.

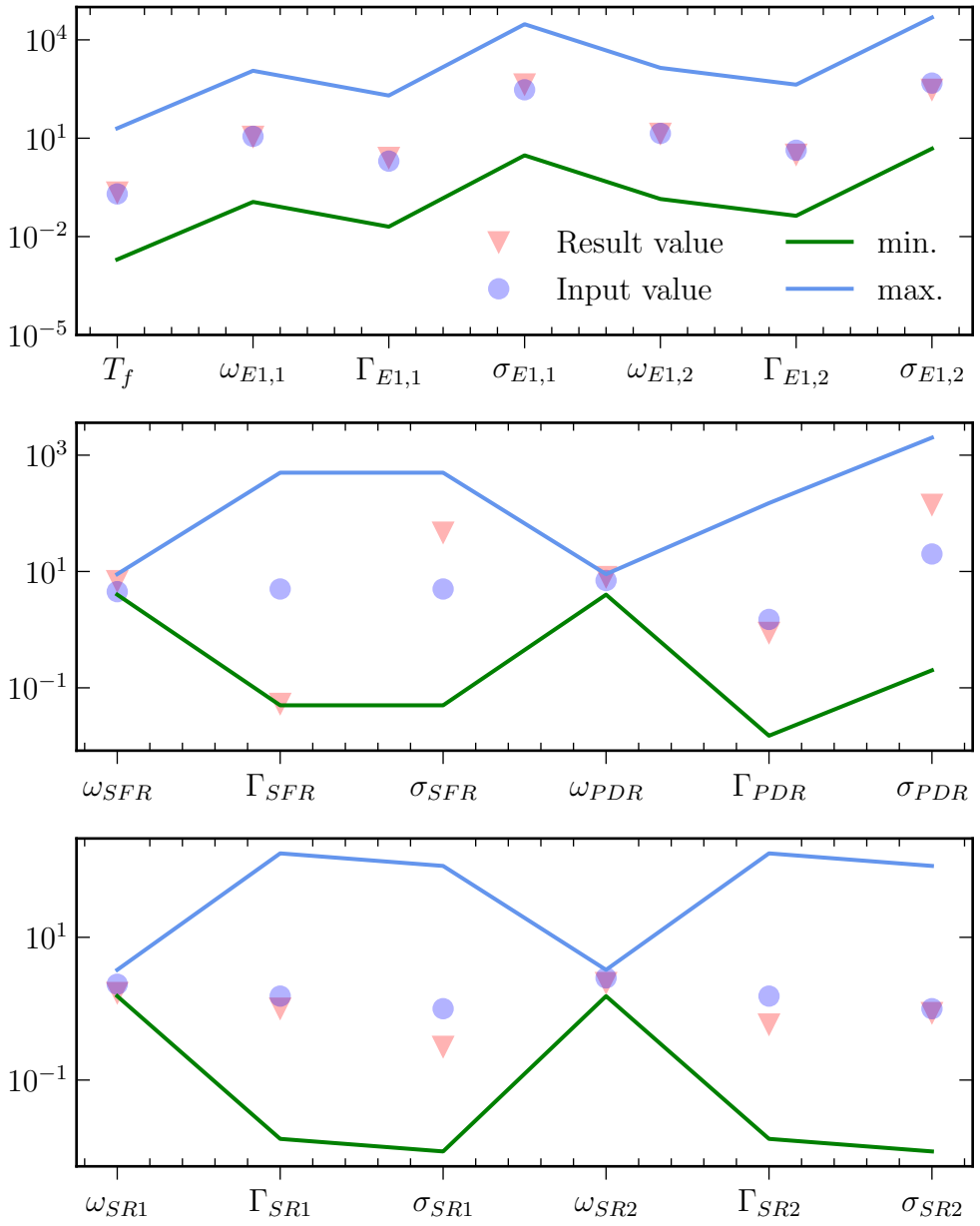


Figure 5.6: Input values to the fit are plotted with blue circles and the resulting values are plotted with red triangles. Upper blue line and lower green line shows the maximum and minimum allowed parameter value in the fitting procedure. The peak centroid parameters ω_{PDR} , ω_{SFR} , $\omega_{SR,1}$ and $\omega_{SR,2}$ were somewhat constrained inside relevant energy intervals and the rest of the parameters has more or less no constraints.

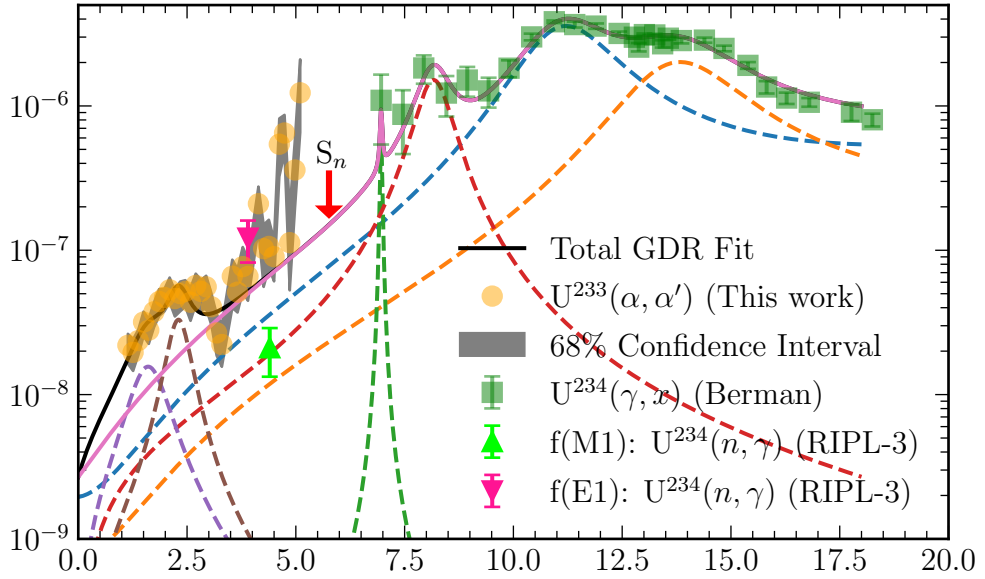


Figure 5.7: The full, less constrained fit of the GDR+PDR+SFR tail is marked with the solid purple line, and the GDR+PDR+SFR+SR fit is marked with the black solid line. The individual fits are all marked with dashed lines.

Table 5.2: The resulting Giant Dipole, Pygmy and Spinflip resonance parameters for the less constrained fit with a 120 keV/bin dispersion. ω , σ and Γ represents the centroid, cross section and FWHM of the given resonance peak. For the GDR fit, the temperature parameter arrived at $T_f = 0.23(102)$ MeV with a large uncertainty. Note the missing uncertainties, which are discussed in the text.

Giant Dipole Resonance					
$\omega_{E1,1}$	$\sigma_{E1,1}$	$\Gamma_{E1,1}$	$\omega_{E1,2}$	$\sigma_{E1,2}$	$\Gamma_{E1,2}$
[MeV]	[mb]	[MeV]	[MeV]	[mb]	[MeV]
11.4(1)	450(63)	2.6(5)	14.08(4)	310(41)	3.2(5)

Pygmy Resonance			Spinflip Resonance		
ω_{PDR}	σ_{PDR}	Γ_{PDR}	ω_{SFR}	σ_{SFR}	Γ_{SFR}
[MeV]	[mb]	[MeV]	[MeV]	[mb]	[MeV]
8.2	143	0.9	6.9	47	0.05

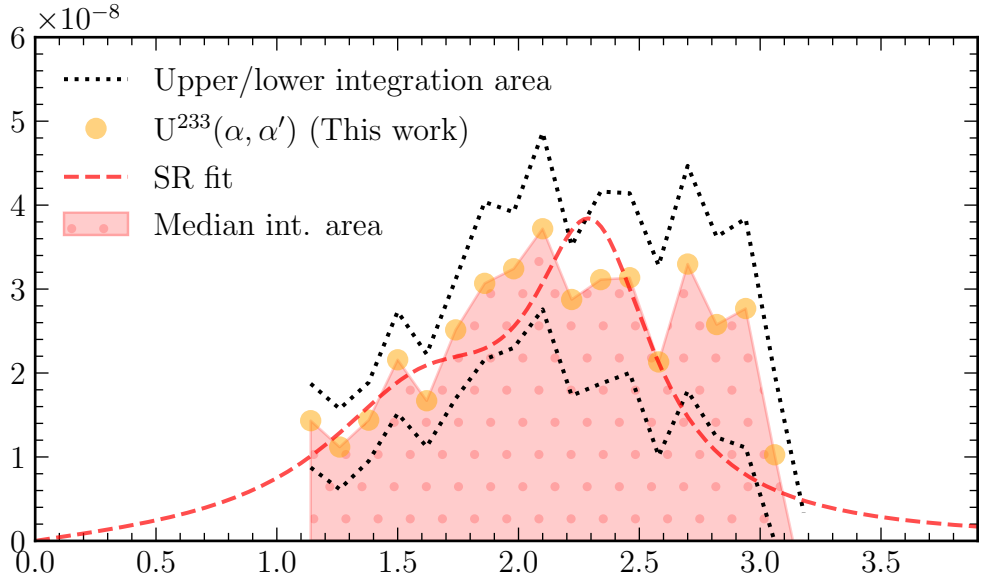


Figure 5.8: The resulting SR mode with the less constrained fit and a 120 keV/bin dispersion is shown as a red stippled line. The red area enclose the integration area used to find the strength of the SR. Black dashed lines show the upper and lower integration areas used to find the uncertainty of the SR strength. Orange circles shows the median γ SF from OMpy with a 120 keV/bin dispersion after the GDR+PDR+SFR tail was subtracted.

The $B_{SR}(M1)$ strength and ω_{SR} centroid from the three different methods are presented in Tab. 5.3 and Fig. 5.9. A deviation between the median $B_{SR}(M1)$ strengths can be seen, although they agree within their errorbars. The ω_{SR} peak centroids are in good agreement.

In Fig. 5.10, the resulting $B_{SR}(M1)$ strengths and ω_{SR} centroids are compared to previous results from Refs. [47, 50–52]. As with Fig. 5.9, the $B_{SR}(M1)$ strengths in the upper panel are in agreement within their errorbars. The ω_{SR} centroids in the lower panel are in good agreement with the previous results.

Table 5.3: *The scissors resonance parameters of ^{233}U . The resonance parameters ω_{SR} and $B_{SR}(M1)$ are the centroid and strength of the resonance. The uncertainty of the strength is represented as a range. The integral range is also presented.*

Scissors Resonance (More constrained)				
Dispersion [keV/bin]	ω_{SR} [MeV]	Integral range [MeV]	$B_{SR}(M1)$ (Median) [μ_N^2]	$B_{SR}(M1)$ (Range) [μ_N^2]
120	2.1(1)	1.2-3.2	7.3	3.1-11.3
185	2.14(5)	1.2-3.2	7.2	4.7-10.2
Scissors Resonance (Less constrained)				
Dispersion [keV/bin]	ω_{SR} [MeV]	Integral range [MeV]	$B_{SR}(M1)$ (Median) [μ_N^2]	$B_{SR}(M1)$ (Range) [μ_N^2]
120	2.2(1)	1.2-3.2	12.6	7.4-17.0

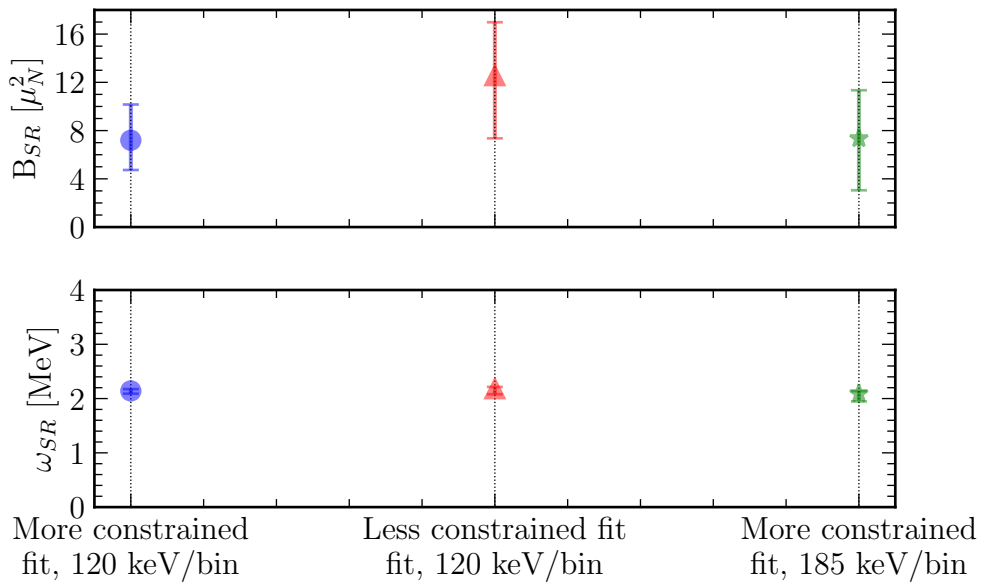


Figure 5.9: *Comparison between the three methods described to measure the SR mode. The less constrained fit is presented with a red triangle. The two other methods are presented with a blue circle (185 keV/bin) and a green star (120 keV/bin). The upper panel shows the $B_{SR}(M1)$ strengths and the lower panel shows the ω_{SR} centroids.*

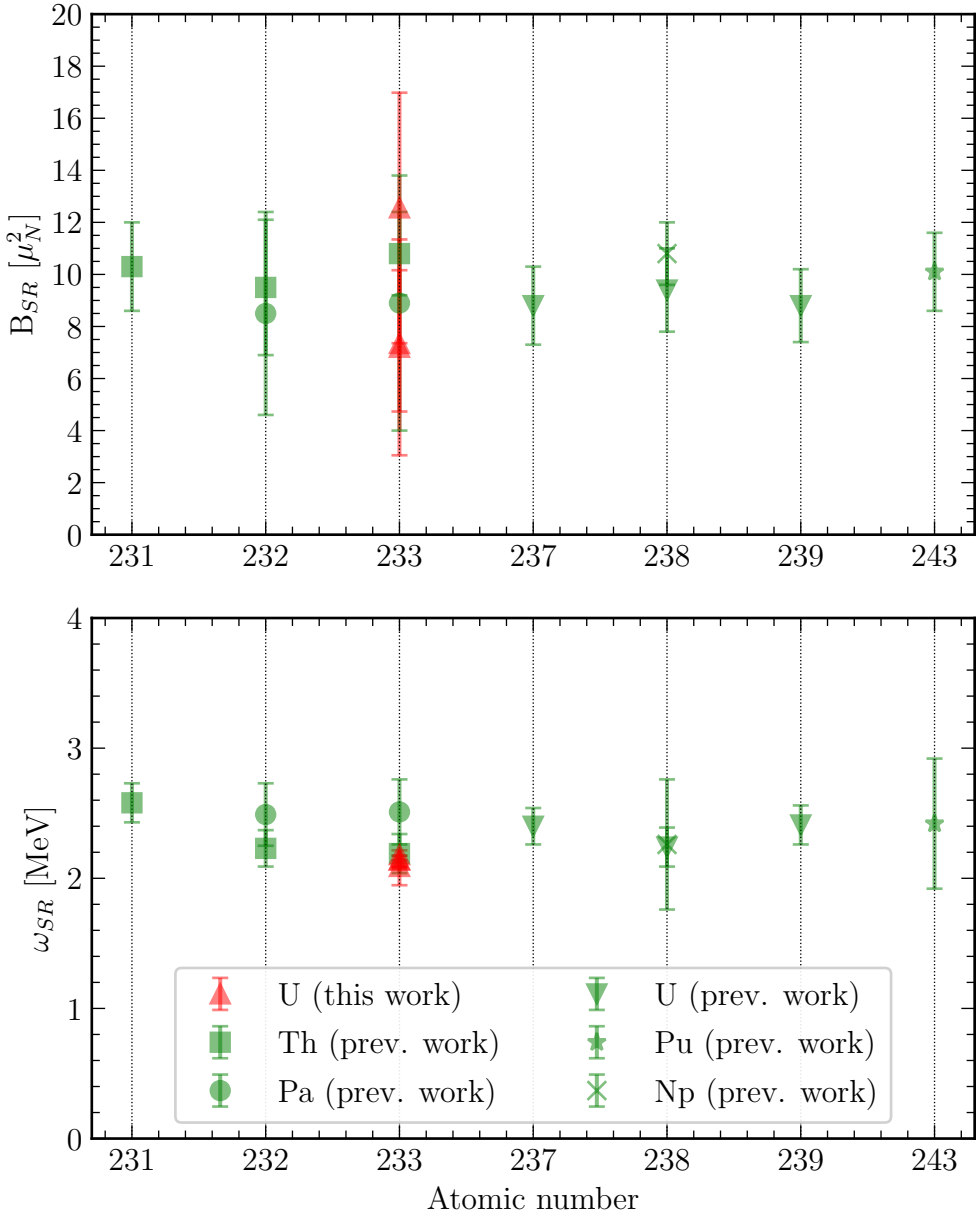


Figure 5.10: Comparison of the SR from this work with previous data from Refs. [47, 50–52]. The $B_{SR}(M1)$ strength are presented in the upper panel and ω_{SR} centroid in the lower panel. The previous data are all marked with green, where equivalent markers represent elements with equivalent proton numbers. Results from the three methods in the presented work is marked with red upward-pointing triangles. The uncertainty from this work comes from integrating the lower/upper boundaries of the γ SF.

5.3 Discussion

5.3.1 NLD and γ SF from the OMpy software

As previously mentioned, this work presents the first Oslo method analysis utilizing the new OMpy software, independent of its authors. Although the software was only recently released, the process of testing is still ongoing. In comparison, the OMS software has been used and tested for almost 20 years. To benchmark the OMpy results in this work, they were compared to the corresponding OMS results.

In wanting to correlate the results from the two software implementations, two energy dispersions were applied in the (E_γ, E_x) coincidence matrix. The resulting NLD from the 185 keV/bin and 120 keV/bin dispersion analysis were in good agreement between OMS and OMpy. For both dispersions, the γ SF also agreed up to approximately 3 MeV. For higher E_γ energies, a slight deviation was found in the resulting γ SF between the OMpy and OMS results for the 185 keV/bin dispersion. In this energy region, the experimental (E_γ, E_x) coincidence matrix had fewer counts (typically < 10 counts/bin) than the rest of the matrix. For the 120 keV/bin dispersion, the γ SF correlated well between the OMS and OMpy analysis, except for the two dipping points as a direct result of bins with few or zero counts in the experimental (E_γ, E_x) coincidence matrix.

Treatment of bins with zero counts is not straightforward, and a satisfying solution was not found while creating the OMpy software [53]. In lack of a solution following a proper uncertainty estimation, the authors have left these bins as zero in the ensemble-based analysis. Additionally, by selecting the bin count for each ensemble member following the Poisson distribution, the bins with few counts are relatively more certain through the unfolding, first-generation, and extraction methods. In contrast, OMS puts a default uncertainty on the zero-count bins. Until a method of treating the bins with few counts is implemented in the OMpy software, the method of leaving out the dips proved to be the best way to correlate the OMpy and OMS methods in this work.

In addition to this unfinished implementation, some difficulties concerning the normalization procedure were uncovered. It was found that the initial definition of the log-likelihood priors of the normalization parameters could facilitate erroneous estimates in the OMpy normalization procedure. Although the origin of this issue is left unsolved, it was avoided in the interest of producing satisfying results. The boundary introduced in Sec. 4.2 is discussed and justified in Appendix A and should be taken into consideration for future analysis with the OMpy software.

OMpy is created with modern software development techniques and modularity in mind, allowing the user to easily change and update methods following future discoveries, upgrades, or difficulties, as was done in this work. In exemplifying ease of use and an ongoing development process, involving the

user via GitHub [37, 44], the OMpy software has demonstrated an adequate attempt to modernize the Oslo method analysis.

5.3.2 Scissors Resonance

In discussing the SR results, one needs to distinguish between the presented and previous methods of extracting the $B_{SR}(M1)$ strength. As mentioned in Sec. 2.3, one usually fit the SR with one or two SLo functions (as the red stippled line in Fig. 5.5) and integrate this fitted curve to find the strength.

In this work, the strength is found by integrating the γ SF, after subtracting the GDR tail. In Fig. 5.5 the experimental γ SF is compared to the SR fit represented by the red stippled line. It is obvious that integrating the fitted curve would yield a larger value as it extends further on both sides of the experimental scissors resonance data. A large drop in the γ SF above 3 MeV justifies the method used in this analysis. In Ref. [27] it was shown that the $B_{SR}(M1)$ strength strongly correlates with the integration limits. By integrating the data up to 3 MeV, one leaves out any excess strength that one would get by integrating the fitted curve.

On the other hand, because of experimental constraints, the presented γ SF has no data below 1.2 MeV. One could speculate that γ SF data in this low energy region could result in a larger integral value. The experimental constraints could justify integrating the fitted curve in this low energy region, rather than the experimental γ SF, to include a possible low-energy contribution.

5.4 Concluding Remarks

The NLD and γ SF have been found for the ^{233}U isotope by utilizing the Oslo method. The analysis was conducted with both the standard Oslo method software and its new python implementation OMpy. An investigation of the dispersion in the (E_γ, E_x) first-generation coincidence matrix has been done to avoid areas with few counts. Two dispersions of 120 keV/bin and 185 keV/bin were used.

For lower E_γ energies (1-3 MeV), the γ SF were in agreement between the OMS and OMpy results for the two different dispersions. For E_γ energies above 3 MeV, a deviation between the γ SF from the two different methods was found with the 185 keV/bin dispersion. The γ SF from the 120 keV/bin dispersion analysis were in good agreement between OMS and OMpy, except for two dips originating from bins with few counts in the (E_γ, E_x) coincidence matrix.

The $B_{SR}(M1)$ strength of ^{233}U has been measured and compared to previous data. Three different strengths are presented and while two are in good agreement, the third deviates from the others. Nevertheless, the errorbars of the $B_{SR}(M1)$ strengths were in good agreement, as well as the

ω_{SR} peak centroids, suggesting the presence of a scissors resonance in the ^{233}U nuclei.

5.5 Outlooks

Experimental data on the neutron capture cross-section for ^{232}U is currently not well characterized. In Chp. 1, the importance of this knowledge and the difficulty of doing experiments with this isotope were introduced. The γ SF and NLD of ^{233}U were extracted in this work and could be used as input in nuclear reaction codes, e.g. Talys [54], to find the neutron capture cross-section for ^{232}U . This cross-section can successively be input in astrophysical simulations or advanced nuclear reactor simulations.

Although the ω_{SR} centroid results from this work were relatively certain, the resulting $B_{SR}(\text{M1})$ strengths deviated between different fitting methods. It is believed that this deviation is a consequence of the uncertain fit to the E1/M1 strength underlying the SR structure. At the OCL group, a new software named *gledeLi*⁶ is under development, intending to fit γ SF and NLD likelihoods with a Bayesian framework (Paper V, manuscript in preparation from Ref. [16]). As this software was not completed before the finalization of this work, it has not been utilized, but it should be implemented at a later stage for a more thorough investigation of the $B_{SR}(\text{M1})$ strength of ^{233}U .

It is uncertain whether the lack of data above $E_\gamma = 3$ MeV is due to the properties of ^{233}U , or experimental constraints from the cross-section of the relevant reaction and beam energy. A new experiment could be conducted, focusing on getting more data for higher E_γ energies. In turn, this could yield a more certain fit of the GDR and lower-lying resonances. In 2017 the OCL detector setup was upgraded with 30 LaBr₃(Ce) detectors, creating the new OSCAR detector array [55]. As with CACTUS, the OSCAR array is paired with SiRi and promises more accurate results in future Oslo method analysis.

⁶Gamma-ray strength function and LEvel DEnsity LIkelihoods, denoted as *gledeLi*

Appendix A

Boundaries on the normalization parameter α

As mentioned in Sec. 4.2, the standard log-uniform priors facilitated wrong guesses in the OMpy normalization procedure. In Fig. A.1, the results from one of the ensemble members that facilitated a misleading normalization is presented⁷. This figure shows that the NLD is not extrapolated to $\rho(S_n)$ and accordingly the γ SF looks nothing like expected. While most of the ensemble members made the right guesses, some did not. As a result, unreasonably large uncertainties in the final normalization results were discovered in Fig. A.2. Here, most ensemble members have a reasonable normalization giving a realistic median and upper confidence interval to the NLD and γ SF. Nevertheless, an excessive number of ensemble members produced unreasonable normalization parameters resulting in a considerably large lower range of the 68% confidence interval.

In Fig. A.3, and the zoomed-in version in Fig. A.4, the probability functions and covariances between the normalization parameters are presented. These plots were generated from the same ensemble member as Fig. A.1, before the boundaries was set on α . As one can see, the normalization parameters all have double-humped probability functions, producing two different solutions to the normalization. Since the two probability distributions could be distinguished between and separated in the left panel of Fig. A.4, it was justified to set normalization limits of α between 1-2 to close in on the peak believed to belong to the correct normalization.

⁷It should be noted that all figures presented in this Appendix are generated automatically by the OMpy and MultiNest softwares. Therefore, they are not optimized for viewing in this thesis, though some were modified to increase their axis labels. Still, it was decided to include the figures to illustrate the relevant issues and solutions.

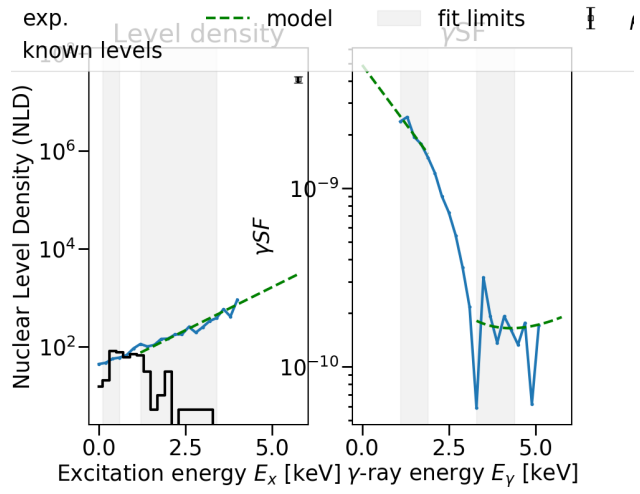


Figure A.1: *OMpy normalization of one of the ensemble members that produced unreasonable normalization results. The left panel shows the NLD and the right panel shows the γ SF. The discrete energy levels are marked with a black solid line and $\rho(S_n)$ with a black square in the left panel. The NLD and γ SF are marked with blue dots and lines. The resulting extrapolations are marked with green, stippled lines and the extrapolation areas with light gray.*

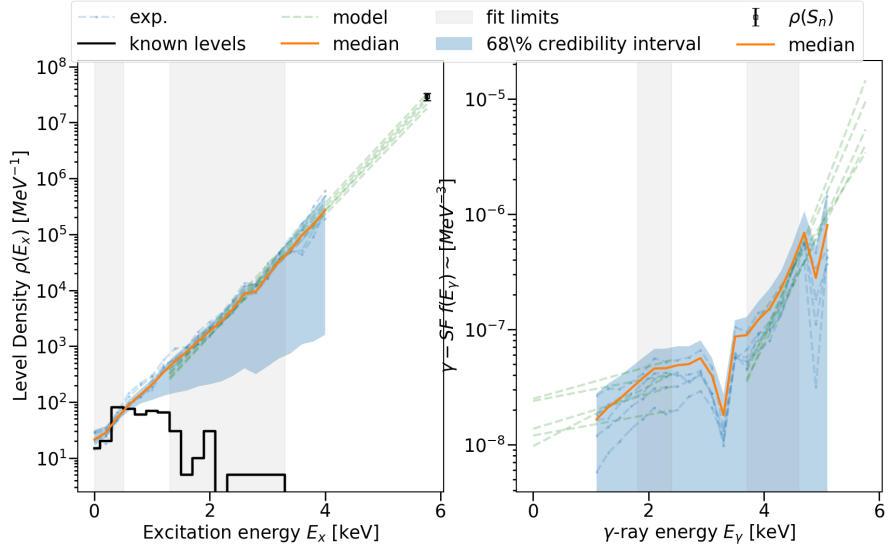


Figure A.2: *OMpy normalizations of the median ensemble member in orange, and a 68% confidence interval in light blue. The left panel shows the NLD and the right panel shows the γ SF. The discrete energy levels are marked with a black solid line and $\rho(S_n)$ with a black square in the left panel. The NLD and γ SF extrapolations are marked with green, stippled lines for a random selection of ensemble members and the extrapolation areas with light gray.*

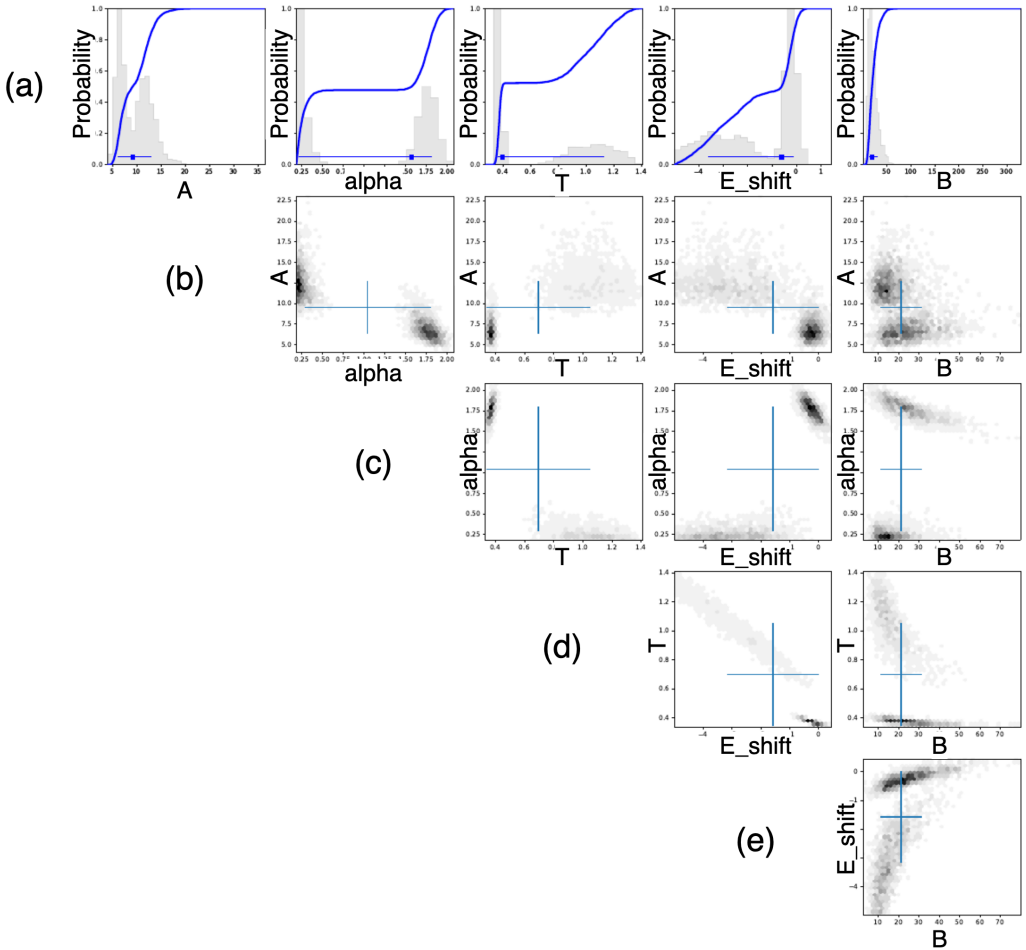


Figure A.3: These plots are generated from the same ensemble member as Fig. A.1. Row (a) shows the five different normalization parameters and their associated probability distributions. Rows (b) to (e) show the covariance between the different normalization parameters. Double humped probability functions can be seen for all the normalization parameters. Also, all the covariances show two different solutions to the normalization for all parameters. The double humped probability function of the normalization parameter B is hard to distinguish in row (a), but the covariance between B and the other parameters indicates that B also has a double humped probability function.

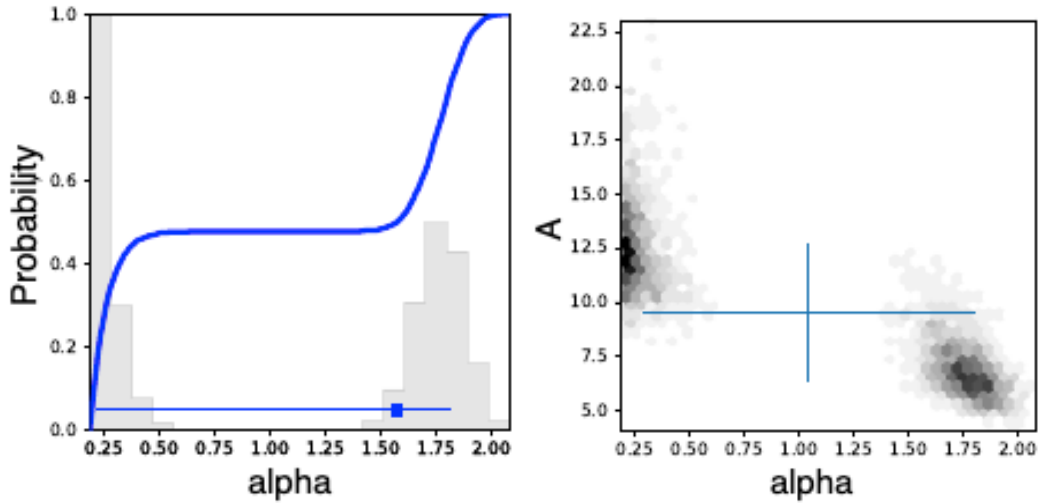


Figure A.4: *The probability distribution of α in the left panel and the covariance between α and A in the right panel, from Fig. A.3. The plots are generated from the same ensemble member as Fig. A.1. The double humped probability distribution of α is obvious. The covariance between the A and α parameters is shown in the right panel, indicating two different solutions to the normalization.*

In Fig. A.5, and the zoomed-in version in Fig. A.6, the normalization parameters are shown, after setting the limits on α for the same ensemble member as in Fig. A.1. Here all the resulting probability functions from the likelihood maximization are normally distributed. This is in better agreement with what was expected from such an analysis.

The reason for the splitting in the probability functions is not fully understood and was not further investigated. Since the normalization parameters are strongly correlated, as can be seen in rows (b)-(e) in Figs. A.3 and A.5, one could speculate that a similar boundary could be set on any of the parameters to produce satisfying results. It was decided to set the boundary on the α parameter, as its probability distribution peaks were the easiest to separate.

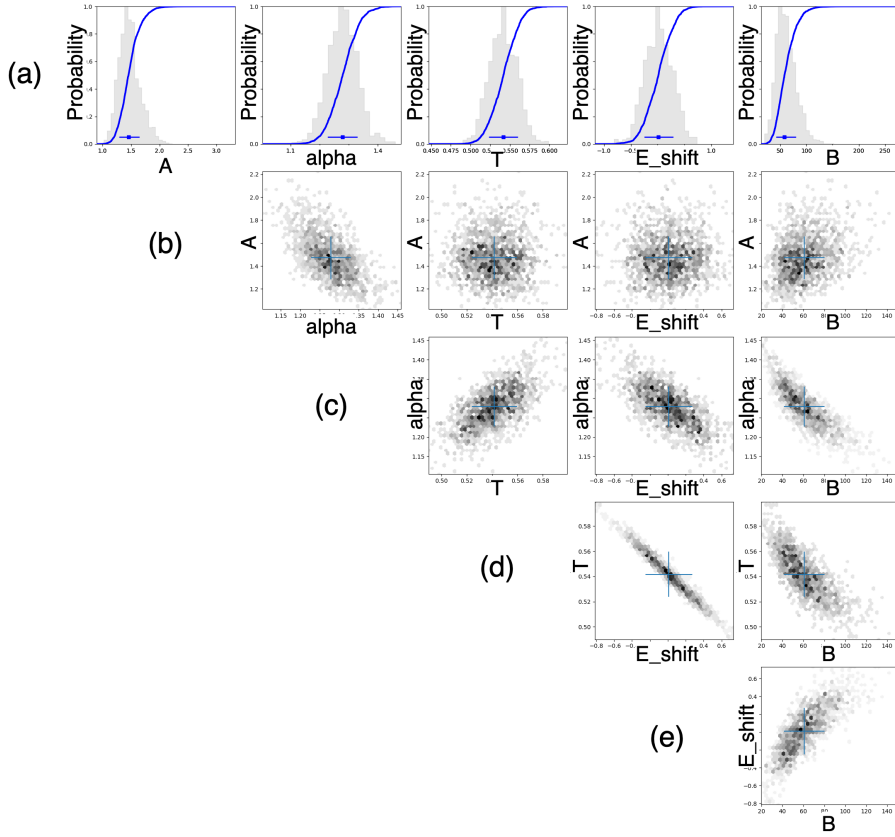


Figure A.5: These plots are generated from the same ensemble member as as Fig. A.1 after the boundary was set on α . Row (a) shows the five different normalization parameters and their associated probability distributions. Rows (b) to (e) show the covariance between the different normalization parameters. In contrast to Fig. A.3, only one solution is found for this normalization.

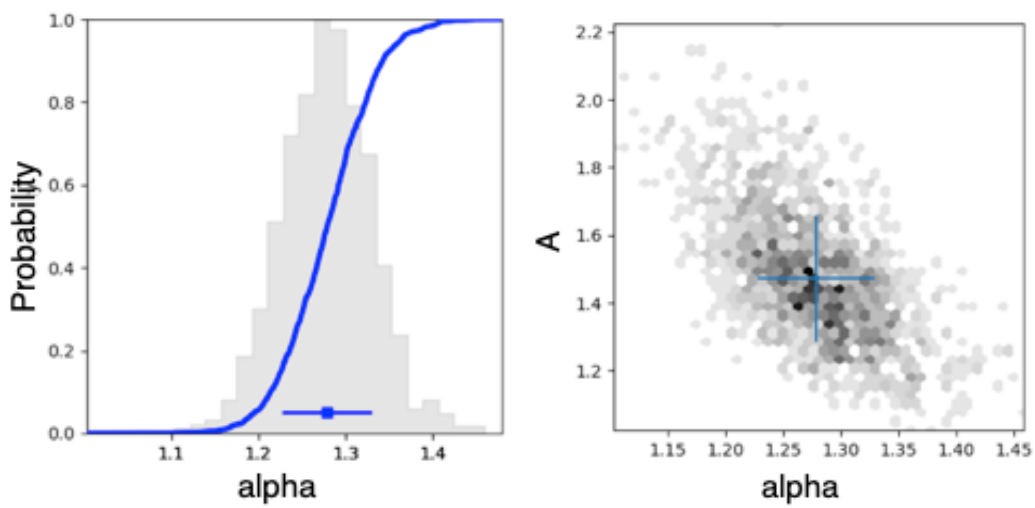


Figure A.6: *The probability distribution of α in the left panel and the covariance between α and A in the right panel, from Fig. A.5. The plots are generated from the same ensemble member as Fig. A.1, after the boundary was set on the α parameter.*

Appendix B

Tables and figures for the more constrained fit with the 185 keV/bin dispersion

As the figures and resonance parameters for the two constrained fits with 185 keV/bin and 120 keV/bin dispersions were rather similar, it was decided to include the 185 keV/bin fit results in this appendix. The SR results were presented in Sec. 5.2.

The following figures illustrates the more constrained fit with a 185 keV/bin dispersion in the (E_γ, E_x) first generation coincidence matrix. Figs. B.1 and B.2 show the GLo and SLo fits to the GDR, PDR, and SFR resonances and their resulting resonance parameters are presented in Tab. B.1. Fig. B.3 show the scissors resonance fit and the integral area used to extract its strength. The resulting $B_{SR}(M1)$ strength and ω_{SR} centroid were presented in Chp. 5, and will not be discussed further in this appendix.

Table B.1: *Giant Dipole, Pygmy and Spinflip resonance parameters for the 185 keV/bin dispersion less constrained results. ω , σ and Γ represents the centroid, cross section and FWHM of the given resonance peak. For the GDR fit, the temperature parameter was fixed at $T_f = 0.2$ MeV.*

Giant Dipole Resonance					
$\omega_{E1,1}$ [MeV]	$\sigma_{E1,1}$ [mb]	$\Gamma_{E1,1}$ [MeV]	$\omega_{E1,2}$ [MeV]	$\sigma_{E1,2}$ [mb]	$\Gamma_{E1,2}$ [MeV]
11.4(2)	453(24)	2.6(5)	14.08(6)	310(37)	3.2(6)
Pygmy Resonance			Spinflip Resonance		
ω_{PDR} [MeV]	σ_{PDR} [mb]	Γ_{PDR} [MeV]	ω_{SF} [MeV]	σ_{SF} [mb]	Γ_{SF} [MeV]
8.17	203	0.5	5.01	13.5	1.5

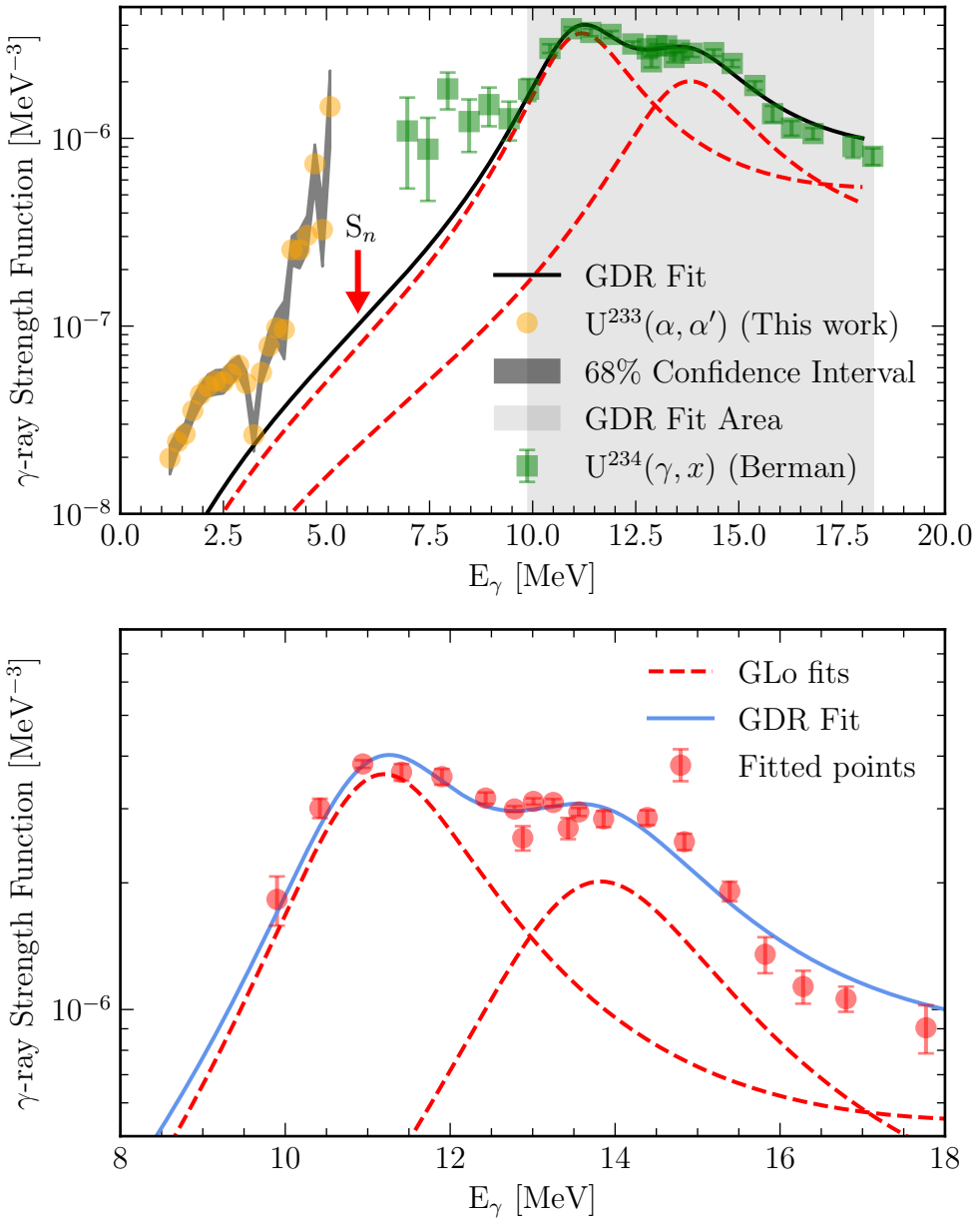


Figure B.1: *Upper panel:* The red stippled lines show the fit of the two GDR peaks and the black solid line shows the total fit for the 185 keV/bin dispersion. The orange circles show the γ SF from this work with a dispersion of 185 keV/bin and its uncertainty as the dark gray 68% confidence interval. The green squares are the cross-section data from Ref. [45] converted to γ SF by Eq. (2.14). The light gray area encloses the energy interval in which the GDR peaks were fit. *Lower panel:* Blue solid line shows the total GDR fit. The red points are the points used in the GDR fit.

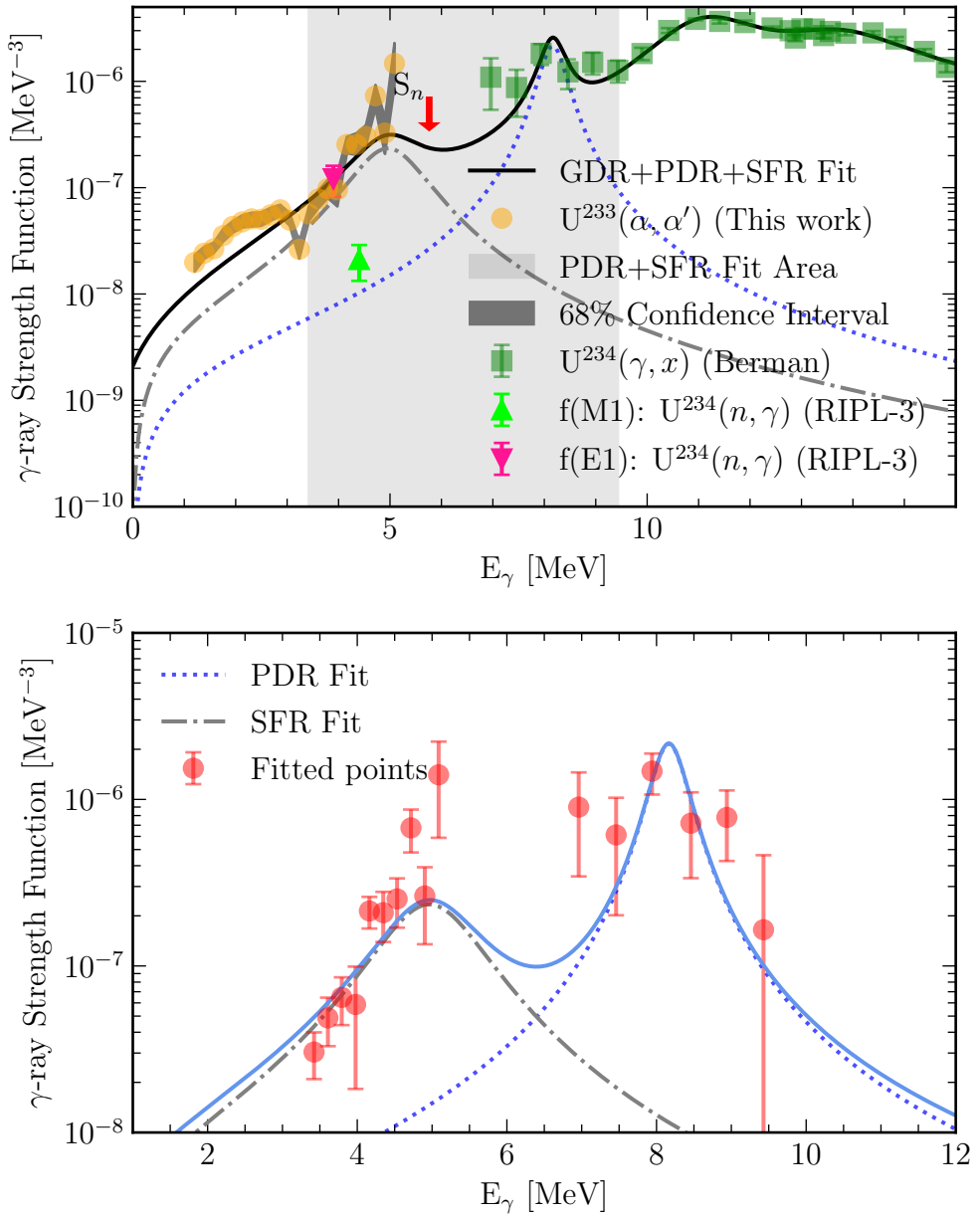


Figure B.2: *Upper panel:* Solid line shows the total GDR+PDR+SFR fit for the 185 keV/bin dispersion. A blue dotted line shows the PDR fit and a grey stippled dotted line shows the SFR fit. The orange circles show the γ SF from this work with a dispersion of 185 keV/bin and its uncertainty as the dark gray 68% confidence interval. The pink and green triangles taken from RIPL-2 data were not used as points in the fit but correlates well with the fit and the data. *Lower panel:* The blue solid line shows the PDR+SFR fit. The red points are a combination of the γ SF from this work and the data from Ref. [45] used to fit the PDR and SFR.

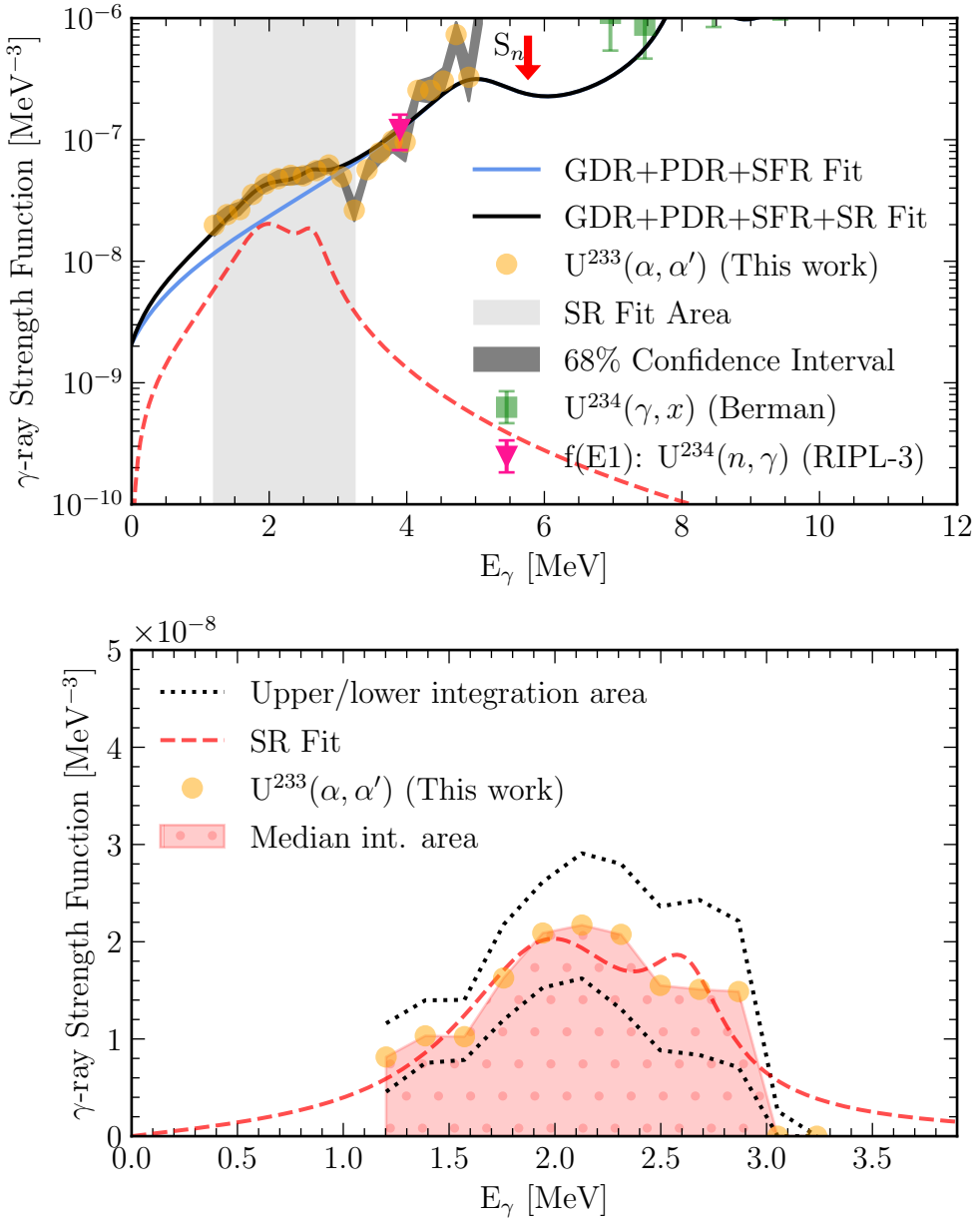


Figure B.3: Upper panel: Black solid line shows the total $GDR+PDR+SFR+SR$ fit for the 185 keV/bin dispersion and in the blue solid line the SR fit is excluded. Lower panel: The red area enclose the integration area used to find the strength of the SR. Black dashed lines show the upper and lower integration areas used to find the uncertainty of the SR strength. Orange circles shows the median γ SF from OMpy with a 185 keV/bin dispersion after the $GDR+PDR+SFR$ tail was subtracted. Note that the fit of the SR is plotted in the upper and lower panel, but it is not used in further analysis.

Bibliography

- [1] NNDC, *National nuclear data center: Nudat 2.8.* [Online]. Available: <https://www.nndc.bnl.gov/nudat2/>, Accessed: 13.04.2021.
- [2] B. P. Abbott, R. Abbott, T. D. Abbott *et al.*, ‘GW170817: Observation of Gravitational Waves from a Binary Neutron Star Inspiral,’ *Physical Review Letters*, vol. 119, no. 16, pp. 30–33, 2017, ISSN: 10797114. DOI: 10.1103/PhysRevLett.119.161101.
- [3] J. Rekstad, A. Henriquez, F. Ingebretsen *et al.*, ‘A Study of the Nuclear Structure at High Energy and Low Spin,’ *Physica Scripta*, vol. 1983, no. T5, pp. 45–50, 1983, ISSN: 14024896. DOI: 10.1088/0031-8949/1983/T5/007.
- [4] L. Henden, L. Bergholt, M. Guttormsen *et al.*, ‘On the relation between the statistical γ -decay and the level density in ^{162}Dy ,’ *Nuclear Physics, Section A*, vol. 589, no. 2, pp. 249–266, 1995, ISSN: 03759474. DOI: 10.1016/0375-9474(95)00133-L.
- [5] T. S. Tveter, L. Bergholt, M. Guttormsen *et al.*, ‘Observation of Fine Structure in Nuclear Level Densities and γ -Ray Strength Functions,’ *Physical Review Letters*, vol. 77, no. 12, pp. 2404–2407, 1996, ISSN: 10797114. DOI: 10.1103/PhysRevLett.77.2404.
- [6] A. Schiller, L. Bergholt, M. Guttormsen *et al.*, ‘Extraction of level density and γ strength function from primary γ spectra,’ *Nuclear Instruments and Methods in Physics Research, Section A: Accelerators, Spectrometers, Detectors and Associated Equipment*, vol. 447, no. 3, pp. 498–511, 2000, ISSN: 01689002. DOI: 10.1016/S0168-9002(99)01187-0.
- [7] OCL, *Oslo cyclotron laboratory website.* [Online]. Available: <https://www.mn.uio.no/fysikk/english/research/about/infrastructure/ocl/index.html>, Accessed: 13.05.2020.
- [8] A. C. Larsen, M. Guttormsen, M. Krtička *et al.*, ‘Analysis of possible systematic errors in the Oslo method,’ *Physical Review C - Nuclear Physics*, vol. 83, no. 3, pp. 1–23, 2011, ISSN: 1089490X. DOI: 10.1103/PhysRevC.83.034315.

- [9] J. E. Midtbø, F. Zeiser, E. Lima *et al.*, ‘A new software implementation of the Oslo method with rigorous statistical uncertainty propagation,’ *Computer Physics Communications*, vol. 262, 2021, ISSN: 00104655. DOI: 10.1016/j.cpc.2020.107795. [Online]. Available: <https://doi.org/10.1016/j.cpc.2020.107795>.
- [10] A. Gilbert and A. G. W. Cameron, ‘A Composite Nuclear-Level Density Formula With Shell Corrections,’ *Canadian Journal of Physics*, vol. 43, no. 8, pp. 1446–1496, 1965. DOI: 10.1139/p65-139..
- [11] R. Capote, M. Herman, P. Obložinský *et al.*, ‘RIPL - Reference Input Parameter Library for Calculation of Nuclear Reactions and Nuclear Data Evaluations,’ *Nuclear Data Sheets*, vol. 110, no. 12, pp. 3107–3214, 2009, ISSN: 00903752. DOI: 10.1016/j.nds.2009.10.004.
- [12] G. A. Bartholomew, E. D. Earle, A. J. Ferguson *et al.*, ‘Gamma-Ray Strength Functions,’ in *Advances in Nuclear Physics*, 1973, ch. 4, pp. 229–324. DOI: 10.1007/978-1-4615-9044-6.
- [13] T. Ericson, ‘A statistical analysis of excited nuclear states,’ *Nuclear Physics*, vol. 11, pp. 481–491, 1959, ISSN: 00295582. DOI: 10.1016/0029-5582(59)90291-3.
- [14] T. Von Egidy and D. Bucurescu, ‘Systematics of nuclear level density parameters,’ *Physical Review C - Nuclear Physics*, vol. 72, no. 4, 2005, ISSN: 05562813. DOI: 10.1103/PhysRevC.72.044311.
- [15] J. Eriksson Midtbø, ‘The low-energy enhancement An experimental and theoretical study of nuclear level densities and γ -ray strength functions,’ Ph.D. dissertation, 2019.
- [16] F. Zeiser, ‘Uncertainty quantification for nuclear level densities and γ -ray strength functions from the Oslo method and beyond,’ Ph.D. dissertation, 2021.
- [17] P. A. M. Dirac, ‘The quantum theory of the emission and absorption of radiation,’ *Proceedings of the Royal Society of London. Series A, Containing Papers of a Mathematical and Physical Character*, vol. 114, no. 767, pp. 243–265, 1927, ISSN: 0950-1207. DOI: 10.1098/rspa.1927.0039.
- [18] P. Axel, ‘Electric dipole ground-state transition width strength function and 7-Mev photon interactions,’ *Physical Review*, vol. 126, no. 2, pp. 671–683, 1962, ISSN: 0031899X. DOI: 10.1103/PhysRev.126.671.
- [19] D. M. Brink, ‘Some aspects of the interaction of fields with matter,’ Doctoral thesis, Balliol College, Oxford, 1955.
- [20] A. Zilges, V. Derya, D. Savran *et al.*, ‘The Pygmy Dipole Resonance—status and new developments,’ *Journal of Physics: Conference Series*, vol. 580, no. 1, 2015, ISSN: 17426596. DOI: 10.1088/1742-6596/580/1/012052.

- [21] K. Heyde, P. Von Neumann-Cosel and A. Richter, ‘Magnetic dipole excitations in nuclei: Elementary modes of nucleonic motion,’ *Reviews of Modern Physics*, vol. 82, no. 3, pp. 2365–2419, 2010, ISSN: 00346861. DOI: 10.1103/RevModPhys.82.2365.
- [22] N. L. Iudice and F. Palumbo, ‘New Isovector Collective Modes in Deformed Nuclei,’ *Physical Review Letters*, vol. 41, no. 22, 1978. DOI: 10.1103/PhysRevLett.41.1532.
- [23] D. Bohle, A. Richter, W. Steffen *et al.*, ‘New magnetic dipole excitation mode studied in the heavy deformed nucleus ^{156}Gd by inelastic electron scattering,’ *Physics Letters B*, vol. 137, no. 1-2, pp. 27–31, 1984, ISSN: 03702693. DOI: 10.1016/0370-2693(84)91099-2.
- [24] Y. Chen and G. A. Leander, ‘Quasicontinuum properties of M1 spectra in the particle-rotor model,’ *Physical Review C*, vol. 26, no. 6, 1982, ISSN: 1098-6596. DOI: 10.1103/PhysRevC.26.2607.
- [25] M. Guttormsen, J. Rekstad, A. Henriquez *et al.*, ‘Nonstatistical Cooling of the Highly Excited ^{161}Dy Nucleus,’ *Physical Review Letters*, vol. 52, no. 2, pp. 2–4, 1984. DOI: 10.1103/PhysRevLett.52.102.
- [26] N. Pietralla, P. Von Brentano, R. D. Herzberg *et al.*, ‘Correlation between low-lying M1 and E2 strength in heavy rare earth nuclei,’ *Physical Review C*, vol. 52, no. 5, pp. 2317–2321, 1995, ISSN: 05562813. DOI: 10.1103/PhysRevC.52.R2317.
- [27] T. Renstrøm, H. Utsunomiya, H. T. Nyhus *et al.*, ‘Verification of detailed balance for γ absorption and emission in Dy isotopes,’ *Physical Review C*, vol. 98, no. 5, pp. 1–14, 2018, ISSN: 24699993. DOI: 10.1103/PhysRevC.98.054310.
- [28] A.-C. Larsen, ‘Statistical properties in the quasi-continuum of atomic nuclei,’ Ph.D. dissertation, 2008.
- [29] S. J. Rose, F. Zeiser, J. N. Wilson *et al.*, ‘Energy dependence of the prompt γ -ray emission from the (d,p)-induced fission of ^{234}U and ^{240}Pu ,’ *Physical Review C*, vol. 96, no. 1, pp. 1–9, 2017, ISSN: 24699993. DOI: 10.1103/PhysRevC.96.014601.
- [30] R. A. Henderson, J. M. Gostic, J. T. Burke *et al.*, ‘Electrodeposition of U and Pu on thin C and Ti substrates,’ *Nuclear Instruments and Methods in Physics Research, Section A: Accelerators, Spectrometers, Detectors and Associated Equipment*, vol. 655, no. 1, pp. 66–71, 2011, ISSN: 01689002. DOI: 10.1016/j.nima.2011.06.023.
- [31] M. Guttormsen, A. Bürger, T. E. Hansen *et al.*, ‘The SiRi particle-telescope system,’ *Nuclear Instruments and Methods in Physics Research, Section A: Accelerators, Spectrometers, Detectors and Associated Equipment*, vol. 648, no. 1, pp. 168–173, 2011, ISSN: 01689002. DOI: 10.1016/j.nima.2011.05.055.

- [32] T. G. Tornyi, A. Görzen, M. Guttormsen *et al.*, ‘A new fission-fragment detector to complement the CACTUS-SiRi setup at the Oslo Cyclotron Laboratory,’ *Nuclear Instruments and Methods in Physics Research, Section A: Accelerators, Spectrometers, Detectors and Associated Equipment*, vol. 738, pp. 6–12, 2014, ISSN: 01689002. DOI: 10.1016/j.nima.2013.12.005. [Online]. Available: <http://dx.doi.org/10.1016/j.nima.2013.12.005>.
- [33] M. Guttormsen, A. Atac, S. Messelt *et al.*, ‘Statistical Gamma-Decay at Low Angular Momentum,’ *Physica Scripta*, vol. 1990, no. T32, pp. 54–60, 1990, ISSN: 14024896. DOI: 10.1088/0031-8949/1990/T32/010.
- [34] V. W. Ingeberg, F. Zeiser and E. Lima, *Oslocyclotronlab/qkinz: Update*, version 1.3.3, Mar. 2018. DOI: 10.5281/zenodo.1206099. [Online]. Available: <https://doi.org/10.5281/zenodo.1206099>.
- [35] M. Guttormsen, T. S. Tveter, L. Bergholt *et al.*, ‘The unfolding of continuum γ -ray spectra,’ *Nuclear Instruments and Methods in Physics Research, Section A: Accelerators, Spectrometers, Detectors and Associated Equipment*, vol. 374, no. 3, pp. 371–376, 1996, ISSN: 01689002. DOI: 10.1016/0168-9002(96)00197-0.
- [36] L. Crespo Campo, F. L. Bello Garrote, T. K. Eriksen *et al.*, ‘Statistical γ -decay properties of Ni 64 and deduced (n,γ) cross section of the s-process branch-point nucleus Ni 63,’ *Physical Review C*, vol. 94, no. 4, pp. 1–11, 2016, ISSN: 24699993. DOI: 10.1103/PhysRevC.94.044321.
- [37] OMPy GitHub page. [Online]. Available: <https://github.com/oslocyclotronlab/ompy>, Accessed: 13.05.2021.
- [38] F. Zeiser, G. M. Tveten, G. Potel *et al.*, ‘Restricted spin-range correction in the Oslo method: The example of nuclear level density and γ -ray strength function from Pu 239 (d,p γ) Pu 240,’ *Physical Review C*, vol. 100, no. 2, pp. 1–9, 2019, ISSN: 24699993. DOI: 10.1103/PhysRevC.100.024305.
- [39] M. Guttormsen, T. Ramsøy and J. Rekstad, ‘The first generation of γ -rays from hot nuclei,’ *Nuclear Inst. and Methods in Physics Research, A*, vol. 255, no. 3, pp. 518–523, 1987, ISSN: 01689002. DOI: 10.1016/0168-9002(87)91221-6.
- [40] T. Von Egidy and D. Bucurescu, ‘Experimental energy-dependent nuclear spin distributions,’ *Physical Review C - Nuclear Physics*, vol. 80, no. 5, pp. 1–19, 2009, ISSN: 1089490X. DOI: 10.1103/PhysRevC.80.054310.
- [41] M. Guttormsen, F. Zeiser, J. E. Midtbø *et al.*, *oslocyclotronlab/oslo-method-software: Oslo Method v1.1.2*, version v1.1.2, Aug. 2018. DOI: 10.5281/zenodo.2318646. [Online]. Available: <https://doi.org/10.5281/zenodo.2318646>.

- [42] Private communications with Magne Guttormsen, Fall 2020/Spring 2021.
- [43] F. Feroz, M. P. Hobson, E. Cameron *et al.*, ‘Importance Nested Sampling and the MultiNest Algorithm,’ *The Open Journal of Astrophysics*, vol. 2, no. 1, pp. 1–17, 2019, ISSN: 2565-6120. DOI: 10.21105/astro.1306.2144.
- [44] J. E. Midtbø, F. Zeiser, E. Lima *et al.*, *Oslocyclotronlab/ompy: OmPy v1.1.0*, version v1.1.0, Jun. 2020. DOI: 10.5281/zenodo.3898281. [Online]. Available: <https://doi.org/10.5281/zenodo.3898281>.
- [45] B. Berman, J. T. Caldwell, E. J. Dowdy *et al.*, ‘Photofission and photoneutron cross sections and photofission neutron multiplicities for ^{233}U , ^{234}U , ^{237}Np , and ^{239}Pu ,’ *Physical Review C*, vol. 34, no. 6, pp. 2201–2214, 1986. DOI: 10.1103/PhysRevC.34.2201. [Online]. Available: <https://link.aps.org/doi/10.1103/PhysRevC.34.2201>.
- [46] T. Belgya, O. Bersillon, R. Capote *et al.*, *Handbook for Calculations of Nuclear Reaction Data, RIPL-2*, June. 2006, ISBN: 92-0-105206-5. [Online]. Available: <http://www-nds.iaea.org/RIPL-2/>.
- [47] M. Guttormsen, L. A. Bernstein, A. Bürger *et al.*, ‘Observation of large scissors resonance strength in actinides,’ *Physical Review Letters*, vol. 109, no. 16, pp. 1–5, 2012, ISSN: 00319007. DOI: 10.1103/PhysRevLett.109.162503.
- [48] K. L. Malatji, K. S. Beckmann, M. Wiedeking *et al.*, ‘Statistical properties of the well deformed Sm 153,155 nuclei and the scissors resonance,’ *Physical Review C*, vol. 103, no. 1, pp. 1–11, 2021, ISSN: 24699993. DOI: 10.1103/PhysRevC.103.014309.
- [49] D. Savran, T. Aumann and A. Zilges, ‘Experimental studies of the Pygmy Dipole Resonance,’ *Progress in Particle and Nuclear Physics*, vol. 70, pp. 210–245, 2013, ISSN: 01466410. DOI: 10.1016/j.ppnp.2013.02.003. [Online]. Available: <http://dx.doi.org/10.1016/j.ppnp.2013.02.003>.
- [50] T. G. Tornyí, M. Guttormsen, T. K. Eriksen *et al.*, ‘Level density and γ -ray strength function in the odd-odd Np 238 nucleus,’ *Physical Review C - Nuclear Physics*, vol. 89, no. 4, pp. 1–8, 2014, ISSN: 1089490X. DOI: 10.1103/PhysRevC.89.044323.
- [51] T. A. Laplace, F. Zeiser, M. Guttormsen *et al.*, ‘Statistical properties of Pu 243, and Pu 242 (n,γ) cross section calculation,’ *Physical Review C*, vol. 93, no. 1, pp. 1–8, 2016, ISSN: 24699993. DOI: 10.1103/PhysRevC.93.014323.
- [52] M. Guttormsen, L. A. Bernstein, A. Görgen *et al.*, ‘Scissors resonance in the quasicontinuum of Th, Pa, and U isotopes,’ *Physical Review C - Nuclear Physics*, vol. 89, no. 1, pp. 1–11, 2014, ISSN: 05562813. DOI: 10.1103/PhysRevC.89.014302.

- [53] Private communications with Fabio Zeiser, Spring 2021.
- [54] A. Koning, S. Hilaire and S. Goriely, ‘Talys-1.9: A nuclear reaction program manual,’ p. 781, 2017.
- [55] F. Zeiser, G. M. Tveten, F. L. Bello Garrote *et al.*, ‘The γ -ray energy response of the Oslo Scintillator Array OSCAR,’ *Nuclear Instruments and Methods in Physics Research, Section A: Accelerators, Spectrometers, Detectors and Associated Equipment*, vol. 985, p. 164 678, 2021, ISSN: 01689002. DOI: 10.1016/j.nima.2020.164678. [Online]. Available: <https://doi.org/10.1016/j.nima.2020.164678>.